TU Delft
Interfacultair Reactor Instituut

IRI 132-93-13

Vortex properties in a strongly texture Bi(2212) high T_c superconductor

P.F.M. Verhoeven

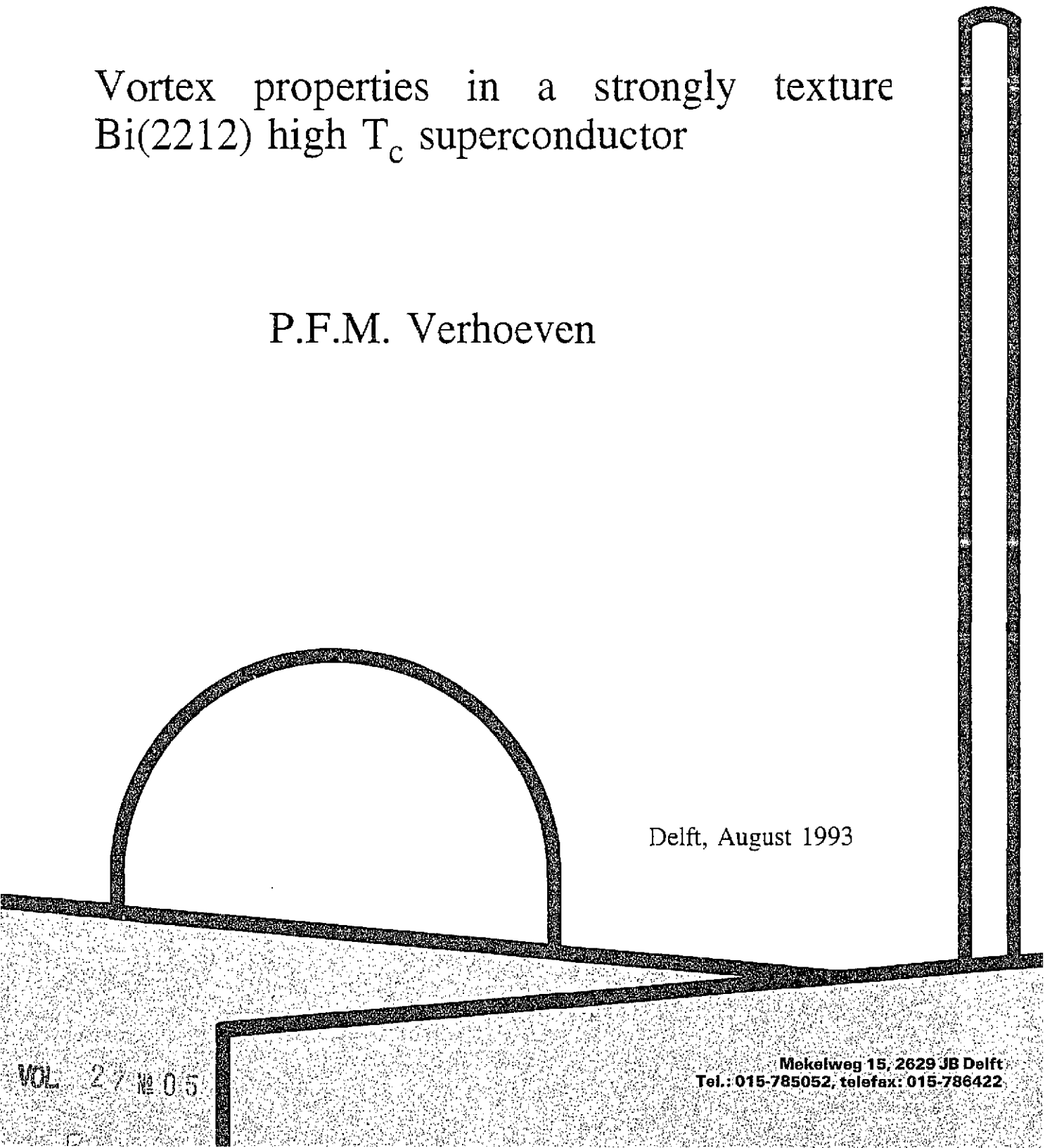

Delft, August 1993

Mekelweg 15, 2629 JB Delft
Tel.: 015-785052, telefax: 015-786422

IRI 132-93-13

Vortex properties in a strongly textured Bi(2212) high T_c superconductor

P.F.M. Verhoeven

Delft, August 1993

Vortex properties of a strongly textured Bi(2212) high T_c superconductor.

P.F.M. Verhoeven

Thesis submitted to the
'Faculteit der Techische Natuurkunde'
of the 'Technische Universiteit Delft'
in partial fulfilment of the
requirements for the degree of
INGENIEUR (ir.)

supervisors:
drs. W. Roest
dr. M. Th. Rekveldt
prof. dr. ir. L.A. de Graaf

Afdeling Stralingsfysica
Interfacultair Reactor Instituut
Technische Universiteit Delft

August 1993

Abstract

The research described in this report was aimed at obtaining more information about the behaviour of vortices in a textured type II $Bi_2Sr_2CaCu_2O_8$ high T_c superconductor. With the neutron depolarization technique used, it is possible to determine the mean magnetic induction in the sample and the magnetic disorder in the vortex system in one measurement. If the mean induction is directed along one of the main axes, it is possible to determine the local orientation of the vortices.

The vortex distribution can in first order approximation be described by the Bean-model. This model claims a constant gradient in the vortex distribution from the edges toward the centre of the superconductor. In order to investigate this gradient, a scan method is used to measure the mean induction as a function of the position in the superconductor. From these measurements a non homogeneous vortex distribution at the edges could be concluded, although it could not be determined whether the gradient of the vortex distribution near the edges is constant.

In order to investigate the relaxation of the vortex distribution after a magnetic field pulse, time dependent measurements were carried out. It appeared that the relaxation of the vortex system on short time scale (ms) is not only due to flux creep, but also to a collective expulsion of vortices because of the repulsive force between the vortices which are very closely packed together right after the pulse.

Large remanence (>20 Gauss) after a large applied field pulse (>1 T) was observed, perpendicular to the applied field. This perpendicular remanence was investigated as a function of time, as a function of position, as a function of temperature and as a function of the applied field pulse. These large perpendicular fields can be explained if the texture of the sample is taken into account.

Samenvatting

Het in dit verslag beschreven onderzoek was gericht op het verkrijgen van meer inzicht in het gedrag van vortices in een getextureerde type II $Bi_2Sr_2CaCu_2O_8$ hoge T_c supergeleider. Voor dit onderzoek is gebruik gemaakt van de neutronen depolarisatie techniek (ND). Met ND is het mogelijk de gemiddelde inductie in de supergeleider over de neutronen bundel en de magnetische chaos in het vortex systeem te bepalen. Tevens kan in sommige gevallen informatie verkregen worden over de lokale oriëntatie van de fluxlijnen.

Het in dit rapport veelvuldig aangehaalde Bean-model beschrijft de vortex distributie in de supergeleider en stelt dat er sprake kan zijn van een constante gradient in de vortex distributie aan de randen van het sample. Om deze gradient te onderzoeken is gebruik gemaakt van een scan methode waarmee de gemiddelde magnetische inductie als functie van de positie in het sample gemeten kon worden. Uit deze scan metingen kwam naar voren dat er inderdaad sprake is van een gradient in de vortex distributie aan de rand, al kon niet worden vastgesteld dat er sprake was van een constante gradient.

Ook zijn er dynamische metingen op korte tijdsschaal (ms) uitgevoerd. Hierbij werd de relaxatie van de vortex verdeling direct na een veldpuls onderzocht. Hieruit volgde dat de relaxatie van de vortexverdeling op korte tijdsschaal niet meer te beschrijven is door alleen uit te gaan flux creep, maar dat er op deze tijdsschaal sprake is van relaxatie t.g.v. het uitzetten van het vortexrooster.

Het bleek dat de remanentie na grote veld pulsen (>1 T) niet alleen gericht was in de richting van het externe veld, maar ook in richtingen loodrecht op dat externe veld. Deze loodrechte remenentie is onderzocht als functie van de positie, de temperatuur, de tijd en de hoogte van de magnetische puls. Tenslotte werden de loodrechte velden verklaard door uit te gaan van de textuur in het sample.

Index

List of symbols

a	Distance between vortices	m
$\mathbf{B}$	Magnetic induction	T
$\langle B \rangle$	Average magnetic induction	T
$\mathbf{B}_{mean}$	Mean magnetic induction caused by vortices	T
c	Neutron constant	$T^{-2}\ m^{-2}$
C_a	Analysing coil system	
C_p	Polarizing coil system	
D	Depolarization matrix	
D'	Depolarization matrix of a volume element	
Det	Neutron detector	
D_c	Calculated depolarization matrix	
D_{ij}	Matrix element ij (ij=xyz) of depolarization matrix	
E_{edge}	Edge energy	$J\ m^{-2}$
$\mathbf{F}$	Force on dipole	N
f_c	Critical pinning force per volume	$N\ m^{-3}$
$\hbar$	Planck's constant	J s
$\mathbf{H}$	Magnetic field	$A\ m^{-1}$
I_{ij}	Detector intensity of depolarization matrix element ij (ij=xyz)	s^{-1}
I_s	Shim intensity of neutron beam	s^{-1}
j	Current density	$A\ m^{-2}$
j_c	Critical current density for flux flow	$A\ m^{-2}$
j_{ca}	Average critical current density for flux flow	$A\ m^{-2}$
j_n	Nett current density due to gradient of vortex distribution	$A\ m^{-2}$
L	Length sample	m
L_s	Partition element sample	m
$\mathbf{M}$	Magnetisation	$A\ m^{-1}$
N	Number of partitions in sample	
N_0	Normalization integral for the calculated matric D_c	m
n_c	Density of Cooper pairs	m^{-2}
n_x, n_y, n_z	Projection of the unit vector of the magnetic induction on the x, y and z axes	
$\mathbf{P}$	Polarization vector	
$\mathbf{P'}$	Polarization vector in volume element	
$\mathbf{P}_i$	Incident polarization vector	
$\mathbf{P}_{i1}$, $\mathbf{P}_{i2}$	Incident polarization vector of sub beams 1 and 2	
$\mathbf{P}_r$	Resulting polarization vector	
$\mathbf{P}_{r1}$, $\mathbf{P}_{r2}$	Resulting polarization vector of sub beams 1 and 2	
r	Radius vortex	m
R_s	Rotation matrix	
S	Volume sample	m^3
$\langle \hat{S}_{x,y,z} \rangle$	Expectation value of neutron spin in magnetic field	J s
t	Time	s
t_1, t_2	Transmission times	s
T_c	Critical temperature for superconductivity	K
x	Distance in sample	m
X_a	Analysing crystal	
X_p	Polarizing crystal	

α_{ij}	Correlation variable describing the correlation along the neutron path between ΔB_i and ΔB_j	$m\ T^2$
β	Angle between external magnetic field and crystallite platelets	
$\Delta\mathbf{B}$	Deviation of the local induction to the average induction	T
$\Delta\lambda$	Width of Gaussian wavelength spectrum in the beam	m
γ_i	Average of the square of the projection of $\Delta\mathbf{B}$ on the denoted axis	
δ_{ij}	Kronecker delta (ij=xyz)	
λ	Penetration depth	m
$\lambda_n,\lambda_1,\lambda_2$	Wavelength of the neutrons	m
ξ_{eff}	Effective penetration length	m
γ_n	Gyromagnetic ratio of the neutron	$s^{-1}\ T^{-1}$
μ_0	Magnetic permeability in vacuum	$H\ m^{-1}$
ρ_v	Density of vortices	m^{-2}
ξ	Correlation parameter proportional to ΔB^2	T
ξ_l	Coherence length	m
τ	Relaxation time for flux creep	s
ϕ	Precession angle of polarization vector	
ϕ_z	Precession angle of polarization vector around the z axis	
χ	Susceptibility	
φ_0	Flux quantum	Wb

1 Introduction

Superconductivity was discovered in 1911 in Leiden by Kamerlingh Onnes [1]. After cooling down pure mercury to a critical temperature T_c of 4.2 K the electrical resistance suddenly disappeared. The absence of electrical resistance is the most prominent property of superconductors. Some other elements also become superconducting beneath their critical temperature T_c, for example aluminium at 1.2 K or niobium at 9.2 K. Some alloys have even higher critical temperatures, for example Nb_3Sn at 23 K.

It was thought for a very long time that much higher critical temperatures were not possible because of prediction by the BCS theory [2], but 1986 brought an important break-through: some ceramic materials with two or more metallic elements plus copperoxide had much higher T_c's. One of these materials is $Bi_2Sr_2CaCu_2O_8$ [3] with a T_c of 90,3 K [4]. This compound was used in the research described in this report.

There is a second important property of superconductors: beneath an external critical field H_{c1}, magnetic flux does not penetrate the bulk of a superconductor. This is called the Meissner effect. At higher fields though magnetic flux does penetrate the bulk of the superconductor. This penetration occurs in a special way. In a superconductor the penetrated flux is quantized. A quantum is called a vortex and contains a flux of $2x10^{-15}$ Wb.

When vortices penetrate they can be pinned by imperfections in the sample. Due to these so called pinning centres some vortices are kept in the superconductor even when the external magnetic field has been removed. This is called the remanent state.

Another consequence of the pinning centres is a gradient in the vortex distribution which depends on the magnetic history of the sample. This vortex distribution can in first order approximation be described by the Bean-model [5].

In the research presented here, the behaviour of the vortices under various conditions, like different temperatures and different magnetic histories, as well as the validity of the Bean-model were studied.

The neutron depolarization technique (ND) was used to study the penetrated vortices. This technique is based on two important properties of neutrons. The first important property is that neutrons hold no charge and so they are not influenced by charge distributions in the sample. The second important property is their spin. This spin implies a magnetic moment which makes them sensitive to magnetic induction. Due to that spin a polarization vector of the neutron beam can be defined.

In a neutron depolarization experiment the influence of the sample on the polarization vector is analyzed [6]. Due to a magnetic induction in the sample, the polarization vector precesses when it travels through the sample. The precession angle is a measure for the mean magnetic induction which is a measure for the vortex density. The shortening of the polarization vector provides information about the fluctuations of the vortex density and the mean local orientation of these fluctuations.

Because of the high transmission of neutrons in matter, ND is a bulk technique so it is possible to measure the induction in the bulk of the superconductor and to obtain information about the fluctuations around the average distribution. This provides an important contribution to the research into the magnetic properties of superconductors which are often done by means of surface or thin film techniques.

2 Theory of superconductors

In 1957 Bardeen, Cooper and Schrieffer [2] found a theoretical explanation for superconductivity known as the BCS-theory. This theory claims an attractive force via phonons between pairs of electrons called **Cooper-pairs**. These electrons are the superconducting charge carriers. For some time this theory explained most effects observed in superconductors. However in 1986, as high T_c superconductors were discovered, it became clear that the BCS-theory using the phonon interaction was not an applicable theory for these materials because, according to the BCS-theory, superconductivity was not possible in these materials. Unfortunately a satisfactory theory for high T_c superconductivity has not been found yet.

The BCS-theory will not be discussed any further in this report. To describe some properties of superconductors related to the research described in this report, phenomenological theories like the London-theory and the Ginzburg-Landau theory are well usable.

2.1 Critical current, critical temperature and critical field

If a critical current I_c, a critical temperature T_c or a critical field H_c is exceded, the superconductor will be in the normal phase. Figure 2.1 shows the phase diagram of a superconductor as a function of the current I, the field **B** and the temperature T. The surface in figure 2.1 crosses the B, I and T axes at $\mu_0\mathbf{H}_c$, T_c and I_c respectively. Below this surface, the material is in the superconducting state.

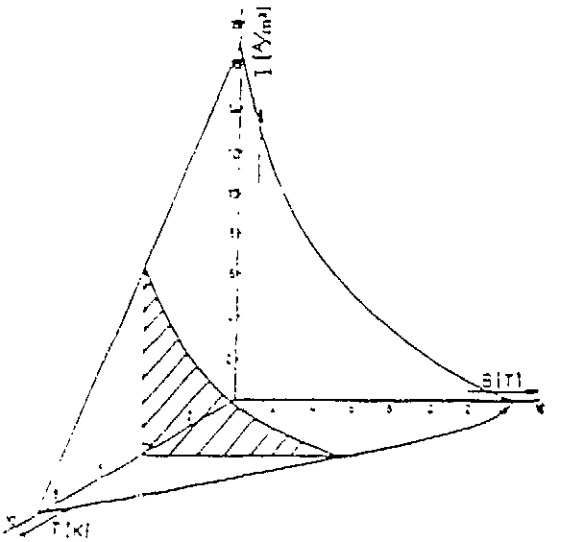

Figure 2.1 Phase diagram of a superconductor as a function of **B**, T and I.

Type I and type II superconductivity

The dotted line in figure 2.2 shows the magnetisation curve of a type I superconductor. There will be no induction (**B**=0) in a type I superconductor if the external field $\mathbf{H}_{ext}$ is

smaller than the critical external field H_c. Therefore in this field region the superconductor acts as a perfect diamagnet. This phenomenon is called the Meissner-effect. The Meissner-effect is due to a circular current of Cooper pairs that flows in an area near the surface of the superconductor. This current causes a magnetic field equal to the external field but in the opposite direction.
In general:

$$B=\mu_0(H+M) \tag{2.1}$$

with

$$M=\chi H \tag{2.2}$$

in a superconductor $B=0$ if $H_{ext}<H_c$, this leads to:

$$\chi=-1 \tag{2.3}$$

this is by definition a perfect diamagnet. Here, **H** is the magnetic field, **B** the induction, **M** the magnetization and χ the susceptibility.

The solid line in figure 2.2 shows the magnetization curve of a type II superconductor. In a type II superconductor flux penetrates the superconductor if H_{ext} exceeds the **lower critical field** H_{c1}. This leads to a decrease of -**M**. Figure 2.2 also shows the **upper critical field** H_{c2}. This is the external field at which the sample will become superconducting if H_{ext} decreases from a field larger than H_{c2}, to a field smaller than H_{c2}.

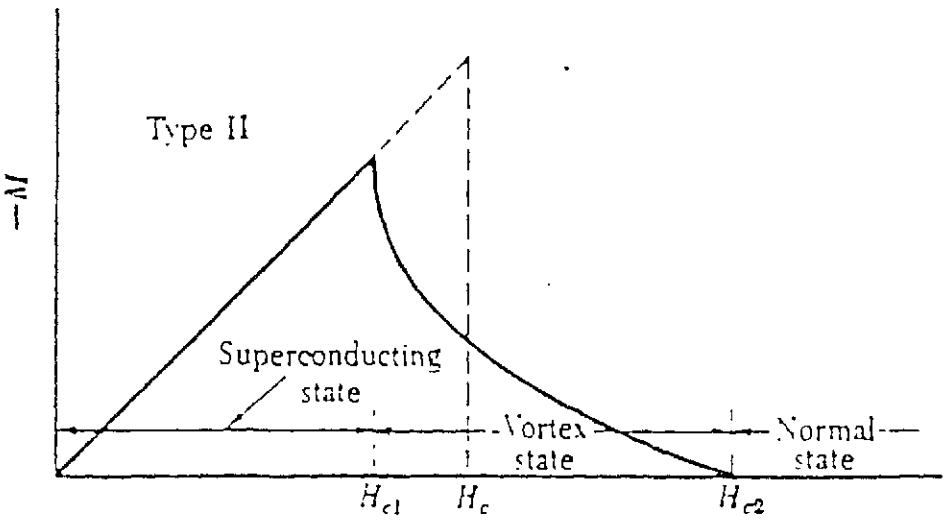

Figure 2.2 Magnetisation **M** as a function of the external field **H** of a type I (dotted line) and a type II superconductor (solid line).

2.2 Vortices.

An external field penetrates the superconductor at the surface over a penetration depth λ in the order of 10^{-7} m. Over this distance the external field drops to zero. Such a region is called a **transistion region.** The penetrated flux changes the energy of such region. This change of energy is called the **edge energy** E_{edge}.

In type I superconductors E_{edge} is positive, in type II superconductors E_{edge} is negative. Because systems tend to minimize their energy, a type I superconductor will try to establish as less transition region as possible as type II superconductors will try to establish as much as possible. Type I superconductors will not be discussed any further because they are of no interest to this report.

At H_{c1}, flux will penetrate the bulk of a type II superconductor in a special way: Type II superconductors will try to maximize the transition region, this can best be done by creating a hollow cylinder of transition region around every infinitesimal amount of penetrated magnetic flux. However the smaliest amount of flux is called a fluxquantum φ_0 and contains $\hbar/2e=2*10^{-15}$ Wb. A cylinder containing one fluxquantum is called a **vortex.**

The centre of a vortex contains a small cylinder that is in the normal phase, this cylinder has a diameter called the **coherence length** ξ_1. The coherence length is equal to the size of a Cooper pair i.e. the distance between the two electrons of a Cooper pair. In this small cylinder the magnetic induction is maximal and constant ($\approx 2\mu_0 H_{c1}$). There is a circular current of Cooper pairs around that small cylinder which shields the magnetic flux in the vortex from the rest of the superconductor. This cylinder has a radius in the order of the penetration depth $\lambda \gg \xi_1$.

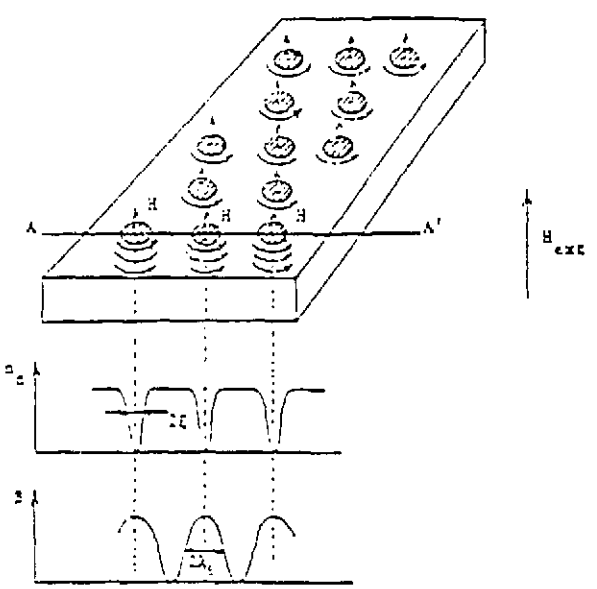

Figure 2.3: Penetration depth λ and coherence length ξ_1 in a cross-section AA' of a vortex lattice. Here n_c is the density of superconducting charge-carriers [7].

When the external field is increased, more vortices will penetrate the bulk of the superconductor: the superconductor is in the so called **mixed state.** If the external field is larger than H_{c2}, the density of vortices will be so high that superconductivity is destroyed.

2.3 Vortex interaction

A current density j exercises a force per unit length on a vortex given by:

$$F = j \times \varphi_0 e_{II} \tag{2.4}$$

Here φ_0 is the flux quantum and $\mathbf{e_{II}}$ is a unity vector in the direction of the flux contained by the vortex. The current density J is due to a net current through the sample or to the circular current of an other vortex. The force is repulsive when vortices have the same flux direction. In a superconductor without impurities this repulsion leads to a triangular vortex lattice. Because such a lattice has the lowest energy it is the most stable one. See figure 2.4.

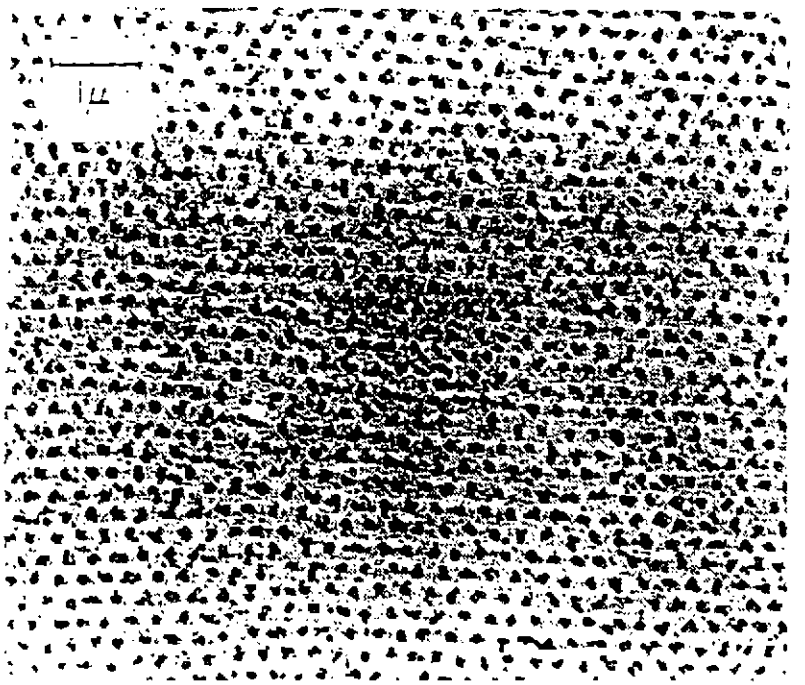

Figure 2.4:Cross-section of triangular vortex lattice in a Pb-In film in a field of $3*10^{-2}$ T. The dots are vortices [7].

When the distance between the vortices in a triangular vortex lattice is a and the density of vortices is ρ_v (=number of vortices per area perpendicular to vortex) the mean magnetic induction in the sample $\mathbf{B}_{mean}$ can be written as:

$$B_{mean} = \rho_v \varphi_0 = \frac{2}{\sqrt{3}} \frac{\varphi_0}{a^2} \tag{2.5}$$

Here $\mathbf{B}_{mean}$ is by definition the mean magnetic induction caused by vortices alone. This is different from average magnetic induction <**B**> measured in the sample holder along the neutron path. Only a fraction of <**B**> is caused by $\mathbf{B}_{mean}$, the rest is caused by the coil and stray fields.

2.4 **Flux-pinning and flux-movement**

Vortices can be pinned by bad regions, like dislocations or impurities, in the superconductor. These regions are called **pinning centres**. This pinning of vortices leads to **remanence** i.e. some vortices remain in the superconductor after a field is applied, even when the external magnetic field is switched off. Pinning centres can be considered as an attractive potential binding the vortices. There is a Boltzmann-like probability that vortices are released by a pinning centre; a rise of temperature increases the release probability. Once vortices are released by a pinning centre, they can move to the next pinning centre, this effect is called **flux creep**.

A current in the superconductor exercises a force $\mathbf{f}_j$ [N m^{-3}] on a vortex lattice. At small currents the pinning centres keep the vortices in position, but at a certain critical current density $\mathbf{j}_c$ the force on the vortex lattice exceeds a critical value f_c [N m^{-3}] and the vortices will start to move, this phenomenon is called **fluxflow**.

2.5 **Bean-model**

Pinning centres lead to a non-homogeneous vortex distribution through-out the sample. This distribution can, in first order approximation, be described by the **Bean-model** [5].

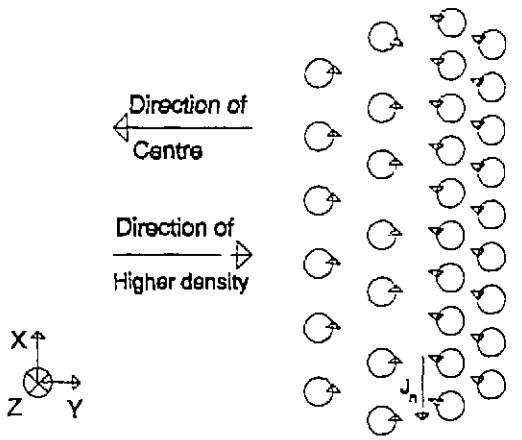

Figure 2.5 Cross-section of vortex lattice. The small circles are vortices. The small arrows indicate the direction of the current around the vortices. $\mathbf{j}_n$ is the net current density.

Imagine a cylindrical superconductor placed in a magnetic field higher than H_{c1}. So that vortices have penetrated the superconductor. Because the vortices are partialy captured by the pinning centres, the density of vortices decreases toward the centre of the sample. In figure 2.5 one can see that this leads to an increasing density of vortices if one goes from the left to the right. This gradient leads to a net tangential current density $\mathbf{j}_n$ in the centre of figure 2.5, because the down-going circular currents due to the vortices in the right half are not entirely compensated by the up-going circular currents due to the vortices in the left half of figure 2.5.

The tangential circular current density $\mathbf{j}_n$ can be written as:

$$j_n = \frac{1}{\mu_0}\frac{d(\varphi_0 \rho_v)}{dr} = \frac{1}{\mu_0}\frac{dB_{mean}}{dr} \tag{2.6}$$

With eq. (2.4) the force per unit volume on a bundle of the vortices in this volume $\mathbf{f}_j$ is then found to be:

$$f_j = \frac{1}{\mu_0}\left(\frac{dB_{mean}}{dr}\right)B_{mean} \tag{2.7}$$

This force is directed toward the centre of the cylinder. In a stable situation this force $\mathbf{f}_j$ is just equal to the maximum force per volume on vortices by the pinning centres, f_c. This results in:

$$\left(\frac{1}{\mu_0}B_{mean}\left(\frac{dB_{mean}}{dr}\right)\right)_{max} = f_c \tag{2.8}$$

The derivative dB_{mean}/dr can only be calculated when f_c/B_{mean} is known.
The Bean-model assumes that the pinning force is constant and homogeneous throughout the sample, hence:

$$\frac{f_c}{B_{mean}} = C \tag{2.9}$$

Using eqs. (2.6), (2.8) and (2.9) leads to:

$$\frac{dB_{mean}}{dr} = \mu_0 C = \mu_0 j_c \tag{2.10}$$

Thus the gradient of the vortex distribution and hence the current density are constant in the critical state.

The next few figures show the consequence of the Bean-model in different situations.

Figure 2.6 shows the vortex distribution, according to the Bean-model, in a superconductor placed in different magnetic fields, after zero field cooling (zfc). At relatively low fields, vortices will not reach the centre of the superconductor (drawn line). At higher fields flux will penetrate deeper, indicated by the dashed- and dotted lines. The dotted line shows a special situation; the external field is so high that vortices reach the centre.

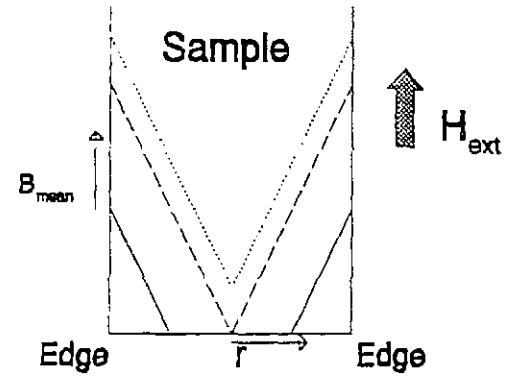

Figure 2.6:Vortex distribution after zero field cooling downto $T<T_c$ and application an external field.

Figure 2.7 shows $\mathbf{B}_{mean}$ of a frozen-in field, i.e. the field was switched on at temperatures above T_c, after which the superconductor was cooled down in field to a temperature below T_c. Above T_c flux will penetrate freely. When the external field is homogeneous, the vortex distribution throughout the sample will be homogeneous. At temperatures relatively close to T_c or at $H \sim H_{c2}$, the sample will be fully penetrated by the vortices.

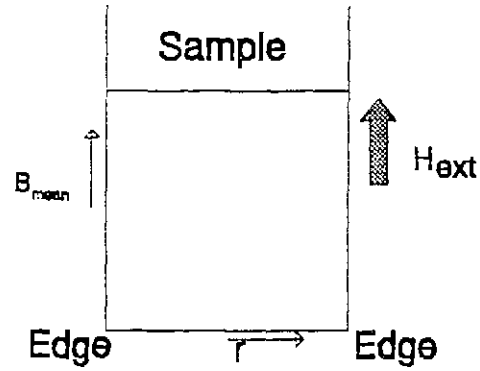

Figure 2.7: Vortex distribution after field cooling downto $T<T_c$.

Figure 2.8 shows the remanence of the frozen-in field of figure 2.7, after the external field has been switched-off. As $\mathbf{B}_{mean}$ at the edge has to be zero there will be an opposite gradient compared to the situation of figure 2.6. In figure 2.6 the force on the vortices due to the external field is directed towards the centre of the sample. Here, the force on the vortices is in the opposite direction due to the higher flux density in the centre. If $\mu_0 \mathbf{H}_{ext} < \mathbf{B}_{saturation}$ in fig. 2.7, the situation of the dotted line excists, after switching of the field.

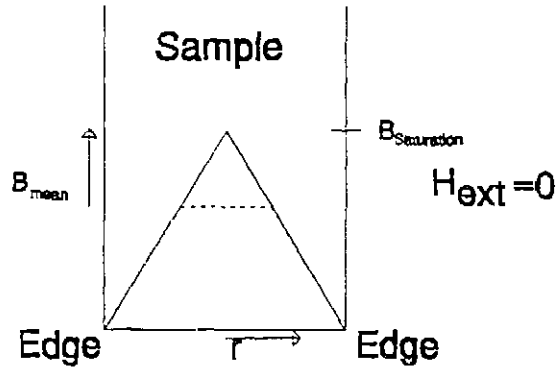

Figure 2.8: Vortex distribution due to the remanence of a frozen-in field.

Figure 2.9 shows the vortex distribution after a field pulse below T_c after zero field cooling downto $T<T_c$. In the beginning of the pulse, vortices will penetrate and the distribution will be a like figure 2.6. When the field decreases at the end of the pulse, vortices will be expelled. This expulsion starts at the edges of the superconductor. Consequently at the edges there will be an opposite gradient which moves deeper into the sample when more vortices leave the superconductor. At the end of this process, when **B**=0 at the edges, there will be two maxima in the distribution at equal distance from the centre. Again with high pulses there is a possibility of vortices reaching the centre (dashed line).

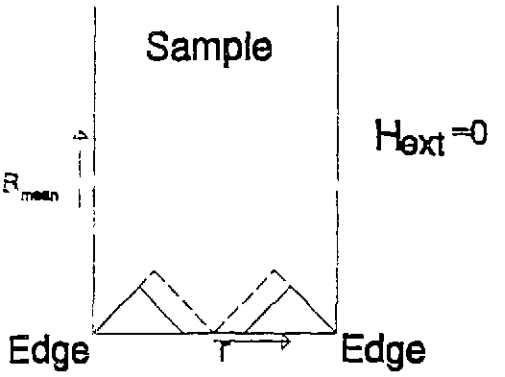

Figure 2.9: Vortex distribution after zero field cooling and a field pulse applied at $T<T_c$.

3 Neutron depolarization technique and theory

With the neutron depolarization technique a polarized neutron beam is transmitted through a sample and analyzed. The technique provides information about the magnetic structure of a sample like the magnetic correlation length which is a measure for the size of a vortex or cluster of vortices. The mean magnetic induction, which is a measure for the vortex density, and the average of the squares of the direction cosines of the local orientation can also be determined.

First some basic theory about the depolarization matrix D will briefly be discussed followed by a description of the crystal polarimeter setup. Furthermore, the neutron depolarization theory will be discussed in more detail. This chapter will be concluded with an explanation of the data-processing method used.

3.1 The depolarization matrix

Neutrons are particles with spin ½ħ which can be directed up or down in a magnetic field. Due to that spin a polarization vector **P** of a neutron beam can be defined:

$$\boldsymbol{P}=(P_x,P_y,P_z)=\left(\frac{\langle\hat{S}_x\rangle}{\tfrac{1}{2}\hbar},\frac{\langle\hat{S}_y\rangle}{\tfrac{1}{2}\hbar},\frac{\langle\hat{S}_z\rangle}{\tfrac{1}{2}\hbar}\right) \tag{3.1}$$

Here $\langle S_{x,y,z}\rangle$ is the expectation value of the spin operator in the x,y and z-direction and ħ is Planck's constant.

The polarization vector **P** changes in time when the neutrons are in a magnetic induction **B**. This change is described by the Larmor-equation:

$$\frac{d\boldsymbol{P}(t)}{dt}=\gamma_n[\boldsymbol{P}(t)\times\boldsymbol{B}(t)] \tag{3.2}$$

Here γ_n is the gyromagnetic ration of a neutron: $\gamma_n=1.8*10^8$ [$s^{-1}T^{-1}$]

The solution of differential equation (3.2) can be found by successive iteration [8]. This leads to:

$$\boldsymbol{P}(t)=\sum_{n=0}^{\infty}\gamma_n\int_0^{t^1}dt^1\ldots\int_0^{t^{n-1}}dt^n[\ldots(\boldsymbol{P}(0)\times\boldsymbol{B}(t^n))\times\ldots\times\boldsymbol{B}(t^1)] \tag{3.3}$$

P is the average polarization vector over all neutron paths in the sample. It is not possible to solve eq. (3.3) analytically, therefore an approximation is made. In this approximation, a so called depolarization matrix D is defined. D transforms the incident polarization vector $\mathbf{P}_i$ into a resulting polarization vector $\mathbf{P}_r$, after transmission.

$$\boldsymbol{P}_r=\boldsymbol{D}\boldsymbol{P}_i \tag{3.4}$$

This depolarization matrix is measured with the crystal polarimeter explained in section 3.2.

3.2 The neutron depolarization technique

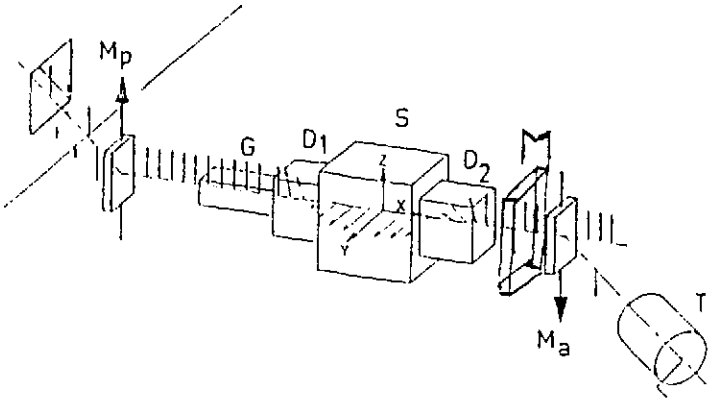

Figure 3.1: The neutron depolarization setup.

Figure 3.1 shows the crystal polarimeter setup. The neutrons enter the polarizing crystal M_p from the left. M_p is a magnetized Heusler (Cu_2MnAl) crystal which separates spin-up and spin-down neutrons. This is possible due to the fact that the magnetic and the nuclear scattering amplitude are equal but have opposite signs for Bragg-reflection in the (111)-direction of Cu_2MnAl for one of the spin directions. In fig. 3.1 this gives constructive interference for spin-up neutron wave functions, i.e. a high intensity of spin-up neutrons, scattered from the (111)-plane, and destructive interference for the neutron wave functions of the spin-down neutrons. In fig. 3.1 the crystal polarimeter is positioned in the (111)-reflection direction (for neutrons with central wave length 0.16 nm) of the Cu_2MnAl. When the crystal is placed in a field in the indicated direction, the total scattering amplitude for the spin down neutron is small so mainly spin up neutrons are reflected. After passing a guide field G, the neutrons reach the coil system D_1 consisting of two coils which are able to rotate the polarization vector in every desired direction by Larmor precession. In practice the polarization vector is directed in the x,y- or z-direction. S is the sample area surrounded by a box of μ-metal to shield-off magnetic stray fields. After the sample area the neutrons pass a second coil system D_2 enabling one to analyze the polarization vector in the x,y or z direction after transmission through the sample. M is a BF_3 neutron monitor that counts a fraction of the neutrons leaving D_2 in order to assure that every matrix element is determined by the same number of neutrons passing the sample. The efficiency of this monitor is 20%. Like M_p, M_a is a magnetized Heusler crystal that reflects a z polarized beam into the neutron detector T. For statistical reasons the setup is placed in the flip condition where the analysed spin direction is opposite to the initial spin direction. Finally the neutrons reach the ^{3}He-detector T that counts the neutrons with flipped spins with an efficiency of 50%.

The elements of the measured depolarization matrix $D_{m,ij}$ are then given by:

$$D_{m,ij}=\frac{1-I_{ij}/I_s}{1-I_{m,ij}/I_s} \qquad i,j=x,y,z \tag{3.5}$$

Here I_{ij} is the neutron detector intensity of a beam polarized in direction j and analyzed in direction i. I_s is the intensity of the fully depolarized beam, called the shim intensity and defined by eq. (3.6).

$$I_s\equiv\frac{I_{ij}+I_{-ij}}{2} \qquad i=x,y,z \tag{3.6}$$

$I_{m,ij}$ is the minimal intensity that can be realized in the ij adjustment of the set up. The denominator is related to the quality of the polarizing/analyzing crystal combination as will be explained later, and has a value of about 0.85.

Before every measurement period of one or two weeks, the analyzing/polarizing systems are calibrated by a third coil-system placed at the sample position. This calibration coil defines the x ,y and z axes.

3.3 Neutron depolarization theory in more detail

3.3.1 Depolarization when <B>=0

The magnetic induction in the sample can be split into the mean magnetic induction in the sample <**B**>, which is assumed to be zero in this case, and the deviation of the local magnetic induction from <**B**>, called $\Delta\boldsymbol{B}$:

$$\boldsymbol{B}=\langle\boldsymbol{B}\rangle+\Delta\boldsymbol{B} \tag{3.7}$$

The time variable t in eq. (3.3) can be transformed into a position variable x using the neutron velocity v_n and the equation $x = v_n t$. Now eq. (3.3) can be written in position coordinates. This is illustrated in figure 3.2:

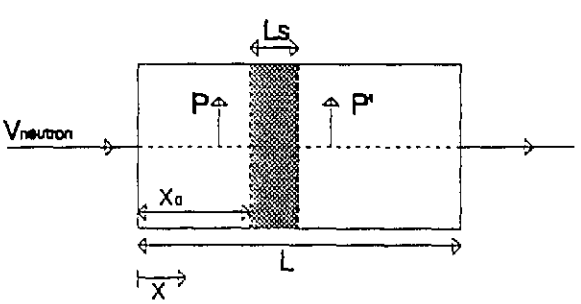

Figure 3.2: The neutron beam in a sample subdivided into N parts L_s. Polarization vector **P** before- and **P'** after transmission through L_s.

The sample with length L is subdivided into N parts with length L_s=L/N. Now equation (3.6) is solved for a part with length L_s. This part is entered by a neutron beam with

polarization vector **P** that is changed into **P'**. It is assumed that $L_s >> \xi$ with ξ the characteristic length of the magnetic correlations and $|\mathbf{P'}-\mathbf{P}| << |\mathbf{P}|$. In other words, the precession in one part is small but caracteristic for the total sample. Under these conditions all third- and higher order terms in (3.3) can be neglected. This results in the following expression for **P'**:

$$\boldsymbol{P'}=\boldsymbol{P}-\frac{cL_s}{V_s}\int_{V_s} d^3\boldsymbol{r}\int_{x_0}^{x} d\boldsymbol{x'}[(\Delta\boldsymbol{B}(\boldsymbol{x})\cdot\Delta\boldsymbol{B}(\boldsymbol{x'}))\boldsymbol{P}-(\boldsymbol{P}\cdot\Delta\boldsymbol{B}(\boldsymbol{x'}))\Delta\boldsymbol{B}] \tag{3.8}$$

Here V_s is the volume of one part, $\Delta\mathbf{B}(x')$ and $\Delta\mathbf{B}(x)$ are shorthand notations for $\Delta\mathbf{B}(x',y,z)$ and $\Delta\mathbf{B}(x,y,z)$ and $c=\gamma_n^2/v_n^2=2{,}18*10^{29}$ $[\lambda_n^2 m^{-1}T^{-2}]$ with λ_n the wave length of the neutrons.

Now the depolarization matrix of volume-element V_s can be written as:

$$\boldsymbol{P'}=\boldsymbol{D'P} \tag{3.9}$$

with D' given by:

$$D'_{ij}=\delta_{ij}(1-cL_s\xi)+cL_s\alpha_{ij} \qquad i,j=x,y,z \tag{3.10}$$

with δ_{ij} the Kronecker-delta. Here is α_{ij} defined by:

$$\alpha_{ij}\equiv\frac{1}{V_s}\int_{V_s} d^3\boldsymbol{r}\int_{x_0}^{x} d\boldsymbol{x'}\Delta B_i(\boldsymbol{x})\cdot\Delta B_j(\boldsymbol{x'}) \qquad i,j=x,y,z \tag{3.11}$$

which is the correlation quantity describing the mean correlation between ΔB_i and ΔB_j along the neutron path and the correlation quantity ξ is defined by:

$$\xi\equiv\sum_{ii}\alpha_{ii} \qquad i=x,y,z \tag{3.12}$$

which is proportional to the correlation length of $\langle\Delta B^2\rangle$ along the neutron path.

The resulting depolarization matrix D of the entire sample can be obtain by multiplying all matrices D' of the partitions. It is assumed that D' is equal in every partition in a homogeneous medium. Then a total sample matrix D is given by:

$$\boldsymbol{D}=(\boldsymbol{D'})^N, \tag{3.13}$$

here $N=L/L_s$. In case D' is diagonal ($\alpha_{ij}=0$ for $i\neq j$) the elements of D will be given by:

$$D_{ij}=\delta_{ij}e^{-cL(\xi-\alpha_{ii})} \qquad i,j=x,y,z \tag{3.14}$$

with $D_{ii}\leq 1$. In an experiment with a magnetically structured sample $D_{ii}<1$, which implies a shortening of the resulting polarization vector $\mathbf{P}_r$ in (3.4), called **depolarization**. Consequently the length of $\mathbf{P}_r$, which depends on D, provides information about magnetic fluctuations in the sample as D is described in terms of α_{ii} which is directly dependent on the magnetic fluctuations.

For $\langle B\rangle=0$, α_{ij} and ξ can be calculated from a measured matrix $D_{m,ij}$ with help of eq. (3.14):

$$\alpha_{ij}=\frac{\ln D_{ij}-\ln(\det(D))/2}{cL} \qquad i,j=x,y,z\ , \tag{3.15}$$

and

$$\xi=-\frac{\ln(\det(D))}{2cL}\ . \tag{3.16}$$

With these two parameters a new parameters γ_i can be defined:

$$\gamma_i=\frac{\alpha_{ij}}{\xi}=1-\frac{2\ln(D_{ij})}{\ln(\det(D))} \qquad i=x,y,z\ , \tag{3.17}$$

which is the average of the square of the projection of ΔB on the denoted direction. γ_i can be approximated by:

$$\gamma_i=\frac{\langle\Delta B_i^2\rangle}{\langle\Delta B^2\rangle}=\langle\cos^2\theta_i\rangle \qquad i=x,y,z \tag{3.18}$$

with θ the angle between ΔB_i and ΔB. The closer γ_i is to 1, the more the magnetic fluctuations are directed in the i direction.

3.3.2 **Depolarization when <B>≠0**

In the case where **<B>**≠0, the polarization vector will undergo a Larmor precession around **<B>**, see figure 3.3:

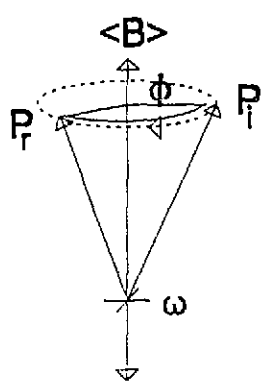

Figure 3.3: Larmor precession of incident polarization vector.

The precession angle ϕ caused by a field distribution with transmission length L is given by:

$$\phi=\omega\cdot t=\sqrt{c}\cdot L\langle B\rangle \tag{3.19}$$

with ω the angular frequency of **P**, t the transmission time and $c=2.18\times10^{29}\times\lambda_n^2$ [$m^{-2}T^{-2}$], with λ_n the wave length of the neutrons.

Because the precession angle in one part ϕ_s is assumed to be small, the depolarization matrix of volume element V_s can be written as a matrix product of a rotation matrix R_s', describing Larmor precession (see eqs. (3.27) and (3.28)), and a depolarization matrix D_s':

$$D'=R_s'(\frac{\phi_s}{2})\ D_s'\ R_s'(\frac{\phi_s}{2}) \tag{3.20}$$

with D_s' given by:

$$D'_{s,ij}=\delta_{ij}e^{-cL_s(\xi+\alpha_{ij})} \qquad i,j=x,y,z \tag{3.21}$$

ξ and α_{ii} are calculated for one part with volume V_s using eq.(3.20) and (3.21). If <**B**> is in the z direction, $\alpha_{ij}=0$ for $i\neq j$ and $\alpha_{xx}=\alpha_{yy}$, the total depolarization matrix D of the sample will be given by:

$$D=(R_s'D_s'R_s')^N=\begin{pmatrix} D_\perp\cos\phi & -D_\perp\sin\phi & 0 \\ D_\perp\sin\phi & D_\perp\cos\phi & 0 \\ 0 & 0 & D_\parallel \end{pmatrix} \tag{3.22}$$

with ϕ the precession angle, $D_\perp$ and $D_\parallel$ the depolarization perpendicular respectively parallel to the z axis. This leads to an expression of the following precession angle ϕ_z around the z axis:

$$\phi_z=\arctan(\frac{D_{xy}-D_{yx}}{D_{xx}+D_{yy}}) \tag{3.23}$$

As ϕ_z can be calculated from D with eq. (3.23), $<B_z>$ can be calculated using (3.19). A simular derivation can be made for $<B_x>$ and $<B_y>$, when the average induction is only in those directions.

With <**B**> and eq. (2.5), the vortexdensity ρ_v can be found:

$$\rho_v=\frac{B_{mean}}{\hbar/2e} \tag{3.24}$$

In case of no external field, there is no Meissner effect and $\mathbf{B}_{mean}$ instead of <**B**> can be used.

3.4 **Data-processing**

Due to the mosaic spread of the polarizing crystal and an angular divergence of the beam there is a wavelength spectrum of the neutrons in the neutron beam. Suppose the neutron beam consists of neutrons with only two different wavelengths (both 50%), implying two different neutron velocities. This leads to two different transmission times, resulting in two different precession angles ϕ_1 and ϕ_2 according to (3.19) where c depends on λ. The incident sub-beams of different wavelengths have parallel polarization vectors $\mathbf{P}_{i,1}$ and $\mathbf{P}_{i,2}$ of equal length leading to a total incident polarization vector $\mathbf{P}_i$ which is the vector average of both $\mathbf{P}_{i,1}$ and $\mathbf{P}_{i,2}$. After transmission, the resulting polarization vectors of the sub-beams $\mathbf{P}_{r,1}$ and $\mathbf{P}_{r,2}$ still have the same lengths but a different direction. Averaging $\mathbf{P}_{r,1}$ and $\mathbf{P}_{r,2}$ gives a

shortened total polarization vector P_r.

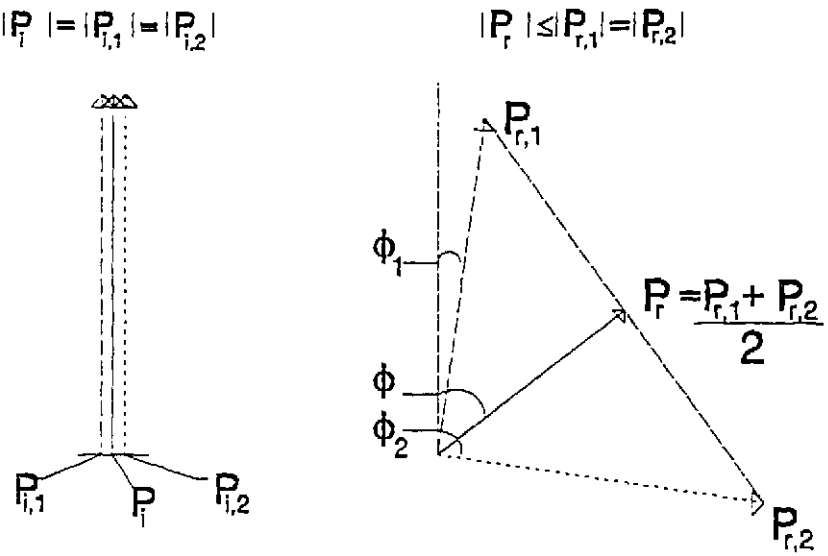

Figure 3.4: Depolarization in a homogeneous field with two discrete wavelengths equally probable in the neutron beam.

Not only the wavelength spectrum but also the quality of the polarizing/analyzing systems and the direction of <B> relative to x,y and z axes influence the measured matrix D_m; this influence is described by quality matrices P and Q for the polarizing and analyzing systems respectively [9]. It is possible to calculate this influence and correct for it. For this purpose an algorithm for numerical correction has been made. The algorithm calculates a simulated matrix D_c from a model. The parameters in D_c are adjusted until $D_c=D_m$ within the statistical errors. The wavelength distribution is assumed to be Gaussian with width $\Delta\lambda$=0.014 nm and central wavelength λ_0=0.16 ± 0.01 nm. The model can then be described by:

$$D_c = N_0^{-1} \int_{-3\Delta\lambda}^{3\Delta\lambda} e^{(\frac{\lambda-\lambda_0}{\Delta\lambda})^2} Q\,(R_s' D_c' R_s')^N\, P\, d\lambda \qquad (3.25)$$

N_0^{-1} normalises the integral and is given by:

$$N_0 = \int_{-3\Delta\lambda}^{3\Delta\lambda} e^{(\frac{\lambda-\lambda_0}{\Delta\lambda})^2} d\lambda \qquad (3.26)$$

Again the sample is divided into N equal parts. R_s' and D_c' are the calculated rotation- and depolarization matrix of one part. In general R_s' can be written as:

$$R_s' = U + S\,\sin\phi + S^2\,(1-\cos\phi) \qquad (3.27)$$

here S is given by:

$$S=\begin{pmatrix} 0 & -n_z & n_y \\ n_z & 0 & -n_x \\ -n_y & n_x & 0 \end{pmatrix} \qquad (3.28)$$

U is a unit matrix, ϕ is the precession angle around the average induction <**B**> and n_i (i=x,y,z) the projections of the unit vector of the magnetic induction on the x,y and z axes. D'_c is the general form of the depolarization matrix in one part given by:

$$D'_c=\begin{pmatrix} 1-cL_s(\alpha_{zz}+\alpha_{yy}) & cL_s\alpha_{xy} & cL_s\alpha_{xz} \\ cL_s\alpha_{xy} & 1-cL_s(\alpha_{zz}+\alpha_{xx}) & cL_s\alpha_{yz} \\ cL_s\alpha_{xz} & cL_s\alpha_{yz} & 1-cL_s(\alpha_{xx}-\alpha_{yy}) \end{pmatrix}. \qquad (3.29)$$

α_{ij} is calculated for one sample part with length L_s using (3,9).

D_c will be adapted to the measured matrix D_m by a least square method. The least square function to be minimized is given by:

$$K=\sum_{i,j=x,y,z}\frac{(D_{c,ij}-D_{m,ij})^2 I_s}{(1-D_{m,ij})(2-D_{m,ij})} \qquad (3.30)$$

This minimization process leads to the following set of parameters: $<B_x>$, $<B_y>$, $<B_z>$, α_{xx}, α_{yy}, α_{zz}, α_{xy}, α_{xz}, α_{yz}. As $\alpha_{ij}=\alpha_{ji}$ all α's are known.

Vortex size

The vortex size is in the order of the effective penetration depth λ_{eff}. With vortices in the z direction and with the assumption that vortices are the only cause for depolarization, λ_{eff} can be written as [9]:

$$\lambda_{eff}=\frac{<B>\varphi_0}{16\alpha_{zz}} \qquad (3.31)$$

with φ_0 the flux quantum. With the remanent <**B**>, which is then equal to $\mathbf{B}_{mean}$ in the order of 10 Gauss, and λ_{eff}=100 nm, the depolarisation ($\equiv$1-| $\mathbf{P}_r$| / | $\mathbf{P}_i$|) is ± 0.018%. This is not measurable, as the minimum depolarization which can be measured is about 0.5%. So no information can be obtained about individual vortices when the vortices are perpendicular to the beam.

Depolarization

If the field in the sample is not directed in the direction of one of the main axes, the method can not distinguish α_{xx}, α_{yy} and α_{zz} because during transmission **P** is no longer along one

main axis. In these cases the average value $<\alpha>$ will be shown. $<\alpha>$ is a measure for the mean magnetic chaos in the system. Unfortunately $<\alpha>$ does not contain information about the direction of the magnetic chaos and so γ_i (i=x,y,z) can not be calculated.

4 Sample and experiment

4.1 The $Bi_2Sr_2CaCu_2O_8$ cell

The structure of the $Bi_2Sr_2CaCu_2O_8$ cell is orthorhombic, which means $|\mathbf{a}|\neq|\mathbf{b}|\neq|\mathbf{c}|$ and $\mathbf{a}\perp\mathbf{b}$, $\mathbf{a}\perp\mathbf{c}$, $\mathbf{b}\perp\mathbf{c}$. Here **a**,**b** and **c** are the lattice vectors, with **c** perpendicular to the CuO-planes (see figure 4.1) in which superconductivity is expected to take place. In these planes much higher super currents of Cooper pairs are possible than in planes perpendicular to the CuO-plane. The lengths of **a**,**b** and **c** are: $|\mathbf{a}|$=0.533 nm, $|\mathbf{b}|$=0.548 nm, $|\mathbf{c}|$=3.076 nm. The critical temperature in the used sample is 90.3 K [4].

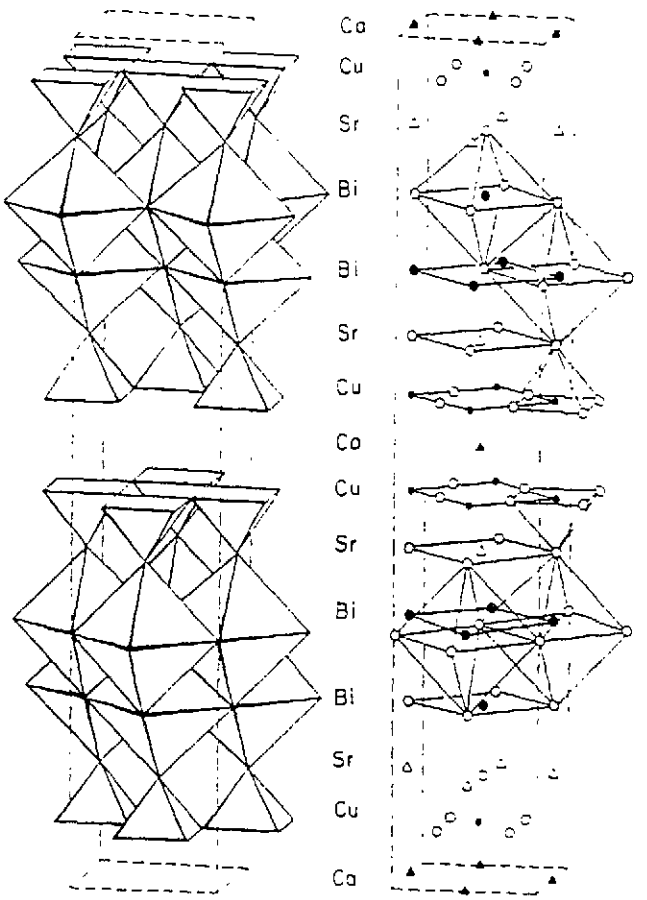

Figure 4.1 The structure of $Bi_2Sr_2CaCu_2O_8$ [10]

4.2 The sample structure

The sample consists of single crystallite $Bi_2Sr_2CaCu_2O_8$ platelets which contain bad regions where only weak super currents of Cooper pairs are possible. These regions can be of different origen for instance dislocations or participates. The thickness of the platelets is about 0.1 mm and the size is more or less arbitrary. In fig. 4.2 a schematic view of the distribution of crystals in the sample is given. The c axis of the crystallite platelets are assumed to be in

the same plane though randomly distributed. There is the possibility of a small distribution of the c-axes around an average direction in the plane.

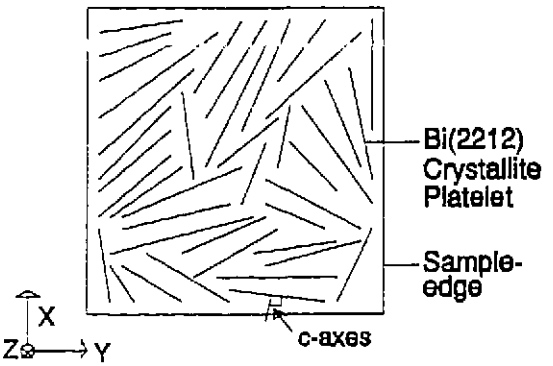

Figure 4.2 Top-view of the sample. Crystallite platelets with the c-axes perpendicular to the platelets and randomly distributed in the x,y plane.

The dimensions of the sample are 6 x 6 x 20 mm^3, with the a axis along the longest direction. The a axis of all crystallite platelets are directed alike. In the measurements, the a axis was meant to be parallel to the z axis as defined after calibration of the crystal polarimeter. In reality there always was a small angle mismatch between the z axis and the a axis

4.3 The sample holder

In figure 4.3, the sample environment in a nitrogen cryostat is given. In the sample holder the sample is placed in a coil which enables one to create an external magnetic field.

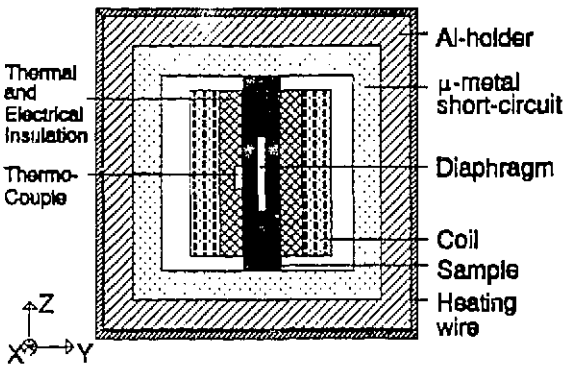

Figure 4.3 Cross-section of the front of the aluminum sample holder with the diaphragm in the centre of the sample. The x direction is the direction of the neutron beam.

The sample is somewhat longer than the coil in order to clamp it between a μ-metal strip which is wrapped around the coil. This strip is necessary to short-circuit the magnetic flux emerging from the coil or the sample outside the neutron beam. Due to this magnetic short-circuit there is only magnetic flux in the sample, in the small space between the sample and the coil and in the μ-metal strip. Therefore the polarization vector of the neutron beam is only influenced by the flux in the beam behind the diaphragm and not by flux emerging from the end of the sample or the coil. This is useful as only the flux in the sample is interesting.

Other useful consequences of the μ-metal strip is that demagnetization fields are avoided and infinitely long fluxlines are simulated.

A possible disadvantage of the μ-metal strip is the possibility of eddy-currents which are circular currents in the metal due to $dH_{ext}/dt \neq 0$. These eddy-currents create magnetic fields that add up to the applied field. This effect has to be kept in mind, especially when the magnetic field is pulsed.

To measure the temperature of the sample, a copper-constantan thermocouple is used. The sensor end of the thermocouple is placed on the sample and thermally and electrically insulated from the coil with teflon tape. The reference part is positioned in a dewar filled with icewater of 273.15 K. The difference in temperature between the two ends, creates a voltage that can be converted into a temperature difference using a table known from literature. The teflon tape is not used inside the beam as this would cause scattering of the neutrons due to the hydrogen in the teflon tape. This scattering would reduce the intensity of the neutron beam. Furthermore, the teflon tape has three important functions:

1 The sample is kept in the centre of the coil by the teflon tape where the field is the most homogeneous and symmetric.
2 There should be no conductive link between the coil and the thermocouple because this could induce a voltage on the thermocouple making accurate temperature measurements impossible.
3 The thermal link between coil and sample should be as small as possible as the temperature of the sample must be independent from the temperature of the coil. Teflon tape is a thermal insulator even at low temperatures.

The temperature of the sample has to be independent from the external magnetic field which depends on the current in the coil. This current increases the temperature of the coil because of Ohmic losses resulting in a temperature increase of the sample as there still is a radiation leak from the coil to the sample. In order to keep the temperature of the sample constant, the sample is heated by a manganin heating wire to a temperature which is somewhat higher than the equilibrium temperature caused by the heating of the coil. A temperature increase of the sample due to heating by the coil is just matched by a temperature decrease caused by less heating by the heating wire, resulting in a constant temperature. The heating wire is wrapped around the sample holder.

Finally, a cadmium diaphragm is used to define the neutron beam. Due to the large absorption cross-section for thermal neutrons in cadmium, only a negligible fraction of the neutrons is transmitted through the cadmium if it is is thick enough. This makes cadmium an ideal material for neutron diaphragms.

4.4 External fields and measurements

The measurements can be split into two different categories. In the first catagory only DC-measurements were carried out, i.e. measurements in a constant external field or after a constant external field was switched off. The first DC-measurements were performed for the purpose of getting a global impression of the responce of the sample to a field and the influence of the external field on the depolarization matrix. In later DC-measurements the local induction will be determined by scanning after zero field cooling (zfc) (the sample temperature is decreased from a temperature $T>T_c$ to $T<T_c$ in zero field after which the field is switched on) and after field cooling (fc) (the temperature is decreased from $T>T_c$ to $T<T_c$ in field) to investigate the applicability of the Bean model.

In the second category, pulse measurements were carried out in order to investigate the

properties of the sample in magnetic fields in the order of Teslas. To achieve these high fields, a large current in the coil (>10 A) is necessary. As the coil is not superconducting, this large current would lead to an unacceptable heating of the sample or to the melting of the copper coil when the current is applied during longer times. For these reasons, the field is pulsed. The large current in the coil (> 10 A) is applied only during a short period of time (ms). The pulse is generated with a pulse generator consisting of four capacitors. Before the pulse, the capacitors are charged to a certain voltage between 25 V and 600 V depending on the desired pulse height. In order to apply a strong current the capacitors are short-circuited over the coil. In the used setup, the pulse duration was about 1 ms. The voltage on the capacitors and the pulse trigger are automatised.

Several types of measurements were performed, after pulse field input. First a scan measurement after a pulse was performed. After that dynamic measurements were carried out in the first 500 ms after a field pulse in order to study the behaviour of the magnetic flux as a function of time. In the last two measurements described, the remanent field was measured as a function of temperature and as a function of the maximum field in the pulse.

In all experiments the pressure in the volume above the liquid nitrogen is lowered in order to reach temperatures down to 65 K.

4.5 Scanning

To get information about the vortex distribution in the sample, the sample is scanned with a narrow neutron beam. To create this beam, a diaphragm is used with dimensions 0.5 x 8 mm^2. The best way of scanning would be to translate the sample perpendicular to the neutron beam before every measurement point. In this way the narrow neutron beam, which is a part of the much wider neutron beam coming from the reactor, is the same in every measurement. This is important as every different neutron beam requires a different calibration of the crystal polarimeter.

A possibility for translational scanning with the same beam configuration is to place the diaphragm outside the cryostat. Unfortunately this means a relatively large distance between diaphragm and sample causing problems due to the angular spread of the neutron beam (0.5°) which results in a beam at the sample position that is much wider than the diaphragm. To adjust for this effect a second diaphragm has to be placed behind the cryostat, reducing the intensity of the beam and thus making measurements more time consuming or less accurate. Because of all these problems, plus the fact that there is simply not enough space to place these two diaphragms outside the cryostat, another scanning method is used. Instead of translating the cryostat, the cryostat is rotated with the diaphragm placed on the rotation axis of the cryostat. In figure 4.4 and 4.5, this scanning method is depicted.

In this way the diaphragm does not move when the cryostat is rotated. This is necessary in order to assure that every measurement is done with the narrow beam configuration. An advantage of this method is the smaller distance between the diaphragm and the sample (30 mm) which leads to less problems caused by the angular spread of the neutron beam. However a disadvantage is the different transmission lengths through the sample for every scan angle. Because it is possible to calculate this difference, this does not lead to real problems. At large scan angles (about 11°) the neutron beam will not leave the sample at the back but at the side. This effect can also be calculated.

Matrices were measured as a function of the scan angles which could be changed by rotating the cryostat. These scan angles can be converted into positions on the centre line of the sample, relative to the side of the sample that was in the beam at φ=0. The diaphragm

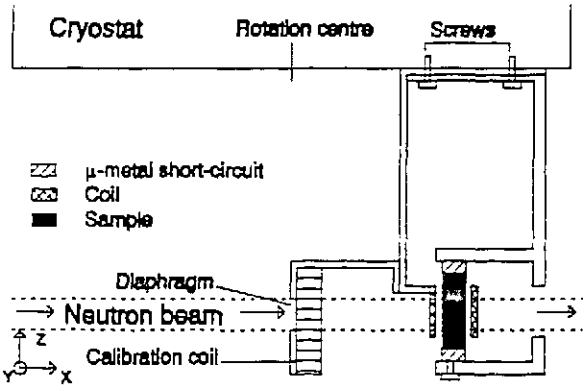

Figure 4.4 Cross-section of side-view of the sample holder with the diaphragm placed in the rotation centre of the cryostat. The calibration coil is placed directly behind the diaphragm.

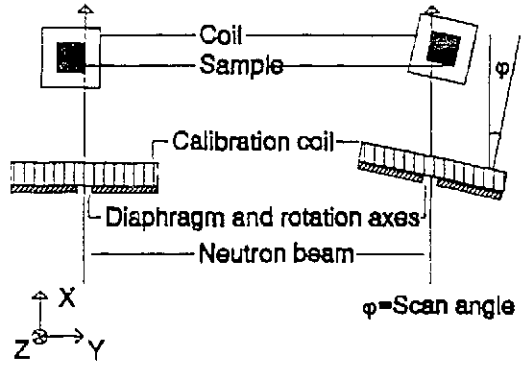

Figure 4.5 Top-view of the rotational scan method with the narrow neutron beam in the x-direction. At the right the sample holder has been rotated over a scan angle φ.

was placed 30 mm in front of the sample, parallel to a sample side because the most interesting effects (gradients in the vortex distribution) were expected to be close to the sample sides. With the assumption that the distribution is symmetric, it was only necessary to get high accuracy in one half of the sample. This could be accomplished by choosing the configuration in figure 4.4. At small angles the transmission length does not change much and the resolution is highest.
in order to reach a temperature of minimal 65 K.

4.6 Hysteresis

In order to get information about the penetration of vortices in an external magnetic field, two hysteresis measurements were carried out at different temperatures, one below T_c and one above T_c. The measurement above T_c is a reference measurement meant to show the difference between the superconductive behaviour and the normal behaviour of the sample. In both experiments a diaphragm of 4 x 8 mm^2 was used. In these experiments the current through the coil is changed by steps of 0.015 A or the external field is changed by steps of 6.45 G, before every measured depolarization matrix. The Gauss per Ampère ratio of the used coil is 430.1 [Gauss/A]. The first matrix is measured without a current in the coil and is used to determine the background field outside the sample. In 20 steps the current through the coil

is increased to 0.3 A resulting in a final external field of 129 Gauss. After decreasing the current in 40 steps to -0.3 A (-129 Gauss), the current is increased again by 40 steps to 0.3 A, in order to close the hysteresis loop. Finally, in the last step, the current is brought back to the starting value of 0 A, to determine the remanent induction (magnetisation).

The temperature is kept constant during the measurements using the method explained in section 4.3. For the measurement below T_c, the temperature is 72.5±1 K. For the reference measurement the temperature is 110±1 K (>T_c).

Before the experiments are started, the ND-apparatus is calibrated by placing a calibration coil at the sample position, instead of the cryostat. This is a different calibration procedure than the one used before the scan measurements. During these measurements the calibration coil was mounted in the cryostat. The calibration procedure determines the quality matrices P and Q, explained in section 3.4, and defines the reference axes x,y and z. The calibration coil used in the hysteresis measurements uses the total neutron beam which is much wider than the neutron beam created by the diaphragms. This results in a non optimal calibration as a different beam from the one used in the experiments, is used during the calibration. The ND-apparatus is calibrated after the removal and replacement of the cryostat before every measurement period of one or two weeks, because it is impossible to place the cryostat on exactly the same position.

5 Results and discussion

5.1 DC-measurements

5.1.1 Hysteresis

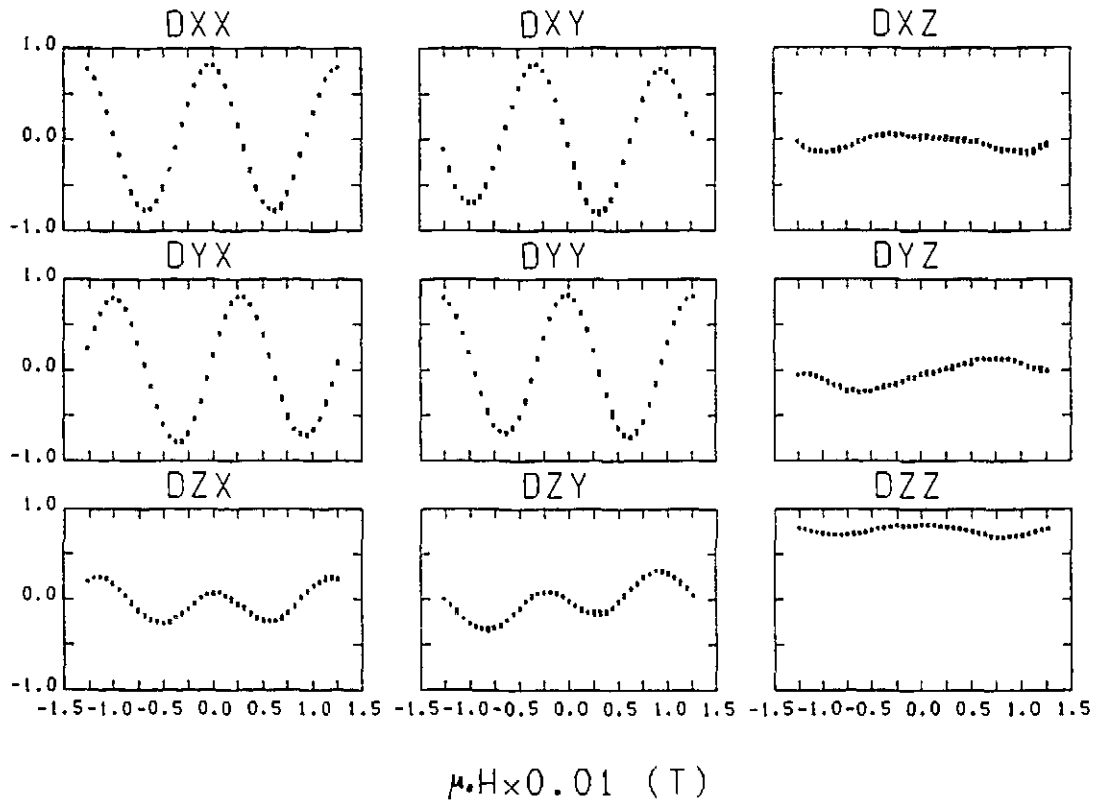

Figure 5.1 The depolarization matrix as a function of the external field at 110 K.

Figures 5.1 and 5.2 show the measured depolarization matrices of a hysteresis measurement at 110 K and 72 K resp. A depolarization matrix can be interpreted with the help of eq. (3.19) and eq. (3.23). In case of a perfectly calibrated system and z-directed magnetic field, only the depolarization matrix elements D_{xx}, D_{xy}, D_{yx} and D_{yy} vary as a function of the magnetic field. D_{xx} and D_{yy} are cosine functions of a magnetic z-field and D_{xy} and D_{yx} are -sinus resp. sinus functions of the z-field. Theoretically the other elements are zero except element D_{zz} which is equal to one. The difference between: D_{xy} and D_{yx}, D_{xz} and D_{zx}, D_{yz} and D_{zy} is a measure for the z, y and x field resp. In figs. 5.1 and 5.2, the elements D_{xz}, D_{yz}, D_{zx}, D_{zy} and D_{zz} are not constant as expected. There are several possible reasons for this:

- Bad positioning of the cryostat in the beam. The diaphragm in the experiment is smaller than the one during the calibration and so the calibration in the experiment might not be optimal.
- An angle between the field in the coil and the z direction, resulting in x- and y-fields. It was quite difficult to direct the coil exactly in the z direction, because due to practical difficulties this had to be done with the bare eye. The x and y fields have to be a linear function of the current in the coil. However this is clearly not the case at a current close to 0.3 A. This effect is probably not relevant because even at large angles (10°), these large

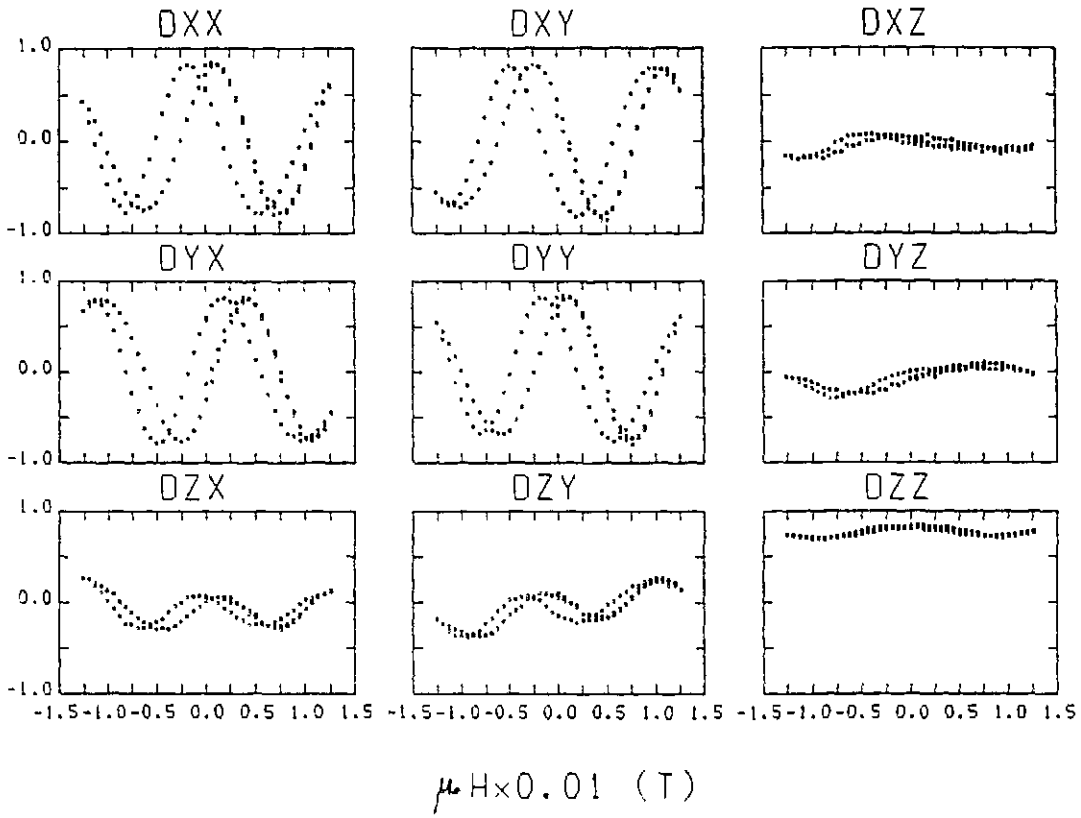

Figure 5.2 The depolarization matrix as a function of the external field at 72.5 K.

effects are not expected.

The first reason is the most likely one. The not symmetric or anti symmetric behaviour of D_{xz}, D_{zx}, D_{yz} and D_{zy} is typical in case of calibration problems.

The matrix element D_{zz} is not equal to it's theoretical value of one because the incoming neutron beam is not fully polarized. As explained before, this is corrected for by the data-processing algorithm described in section 3.4.

Figures 5.3 and 5.4 show that at large external fields, large x and y fields are measured. These fields are not caused by some unexpected behaviour of vortices, because these high x and y fields are also observed in the hysteresis measurement above T_c. The high x and y fields are most probably caused by calibration problems as discussed before. Another effect is that at maximum field, the precession angle ϕ is close to 2π, which gives a problem in the deconvolution. The perfect rotation is only determined $nx2\pi$ (n is an integer) and so the algorithm can not distinguish between 0 and 2π rotation. This could lead to errors in the calculated fields at $\phi \sim 2\pi$.

In the measurement at 110 K, the measured magnetic induction as a function of the current in the coil is somewhat larger than in the measurement at 72.5 K, because above T_c there is no Meissner-effect causing a field opposite to the external field reducing the measured magnetic field. With an external field of 129 Gauss, the difference is about 7 G.

By calculating the magnetic field at zero external field, after the external field was decreased from it's maximum value of 129 G to 0 G, the remanence due to an external field of 129 G can be calculated. In this measurement the remanence is 20 G.

Finally figure 5.5 shows the determinant of the depolarization matrix as function of the current in the coil of the measurement above T_c. This determinant is the third power of the length of the resulting polarization vector which is maximal 0.84 due to a non optimal

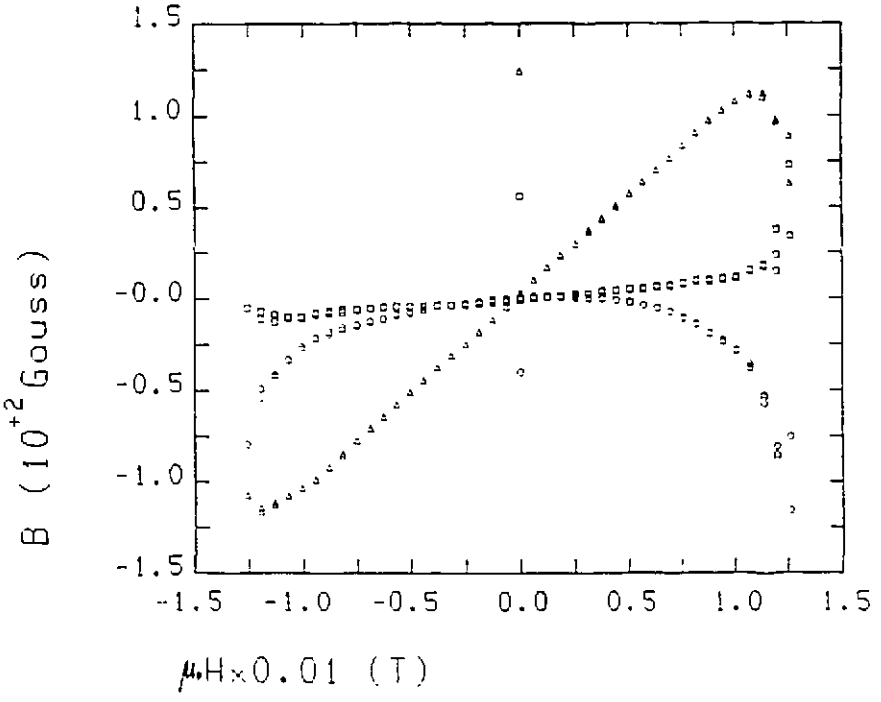

Figure 5.3 The magnetic induction as a function of the external field at 110 K. The squares indicate the x field, the circles indicate the y field and the triangles indicate the z field.

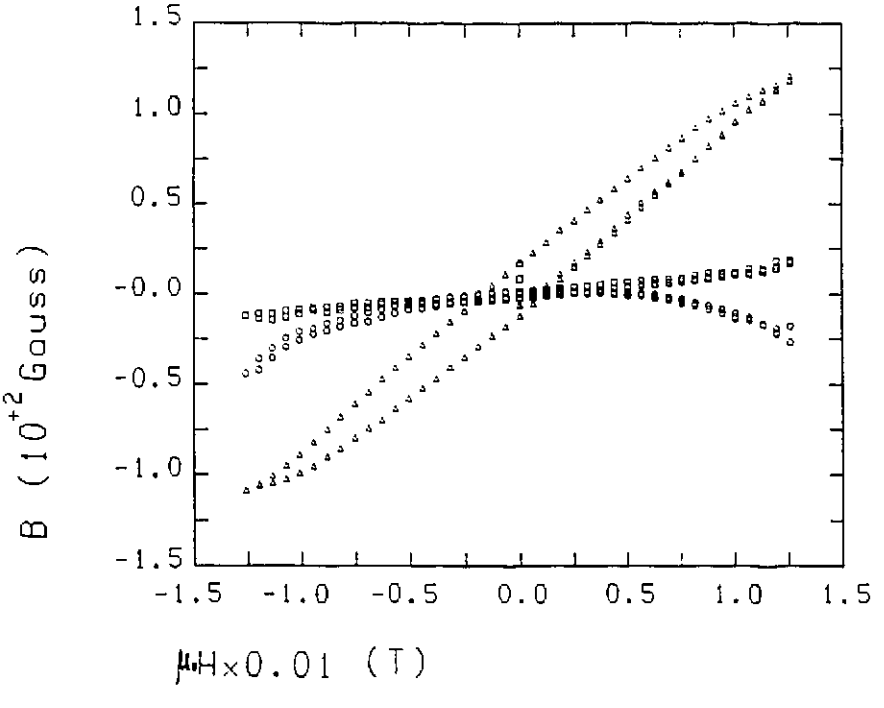

Figure 5.4 The magnetic induction as function of the external field at 72.5 K. The squares indicate the x field, the circles indicate the y field and the triangles indicate the z field.

polarization. If there is no depolarization the determinant is maximal $(0.84)^3$=0.6. The

depolarization, resulting in a smaller determinant, becomes stronger when the external field increases. This is caused by the wavelength spread of the neutrons in the neutron beam. Figure 5.5 showing the depolarization matrix of the hysteresis measurement at 110 K, makes clear that this is a considerable effect that can be corrected for, using the method described in section 3.4. The depolarization matrix of the hysteresis measurement at 72.5 K, gives a simular result.

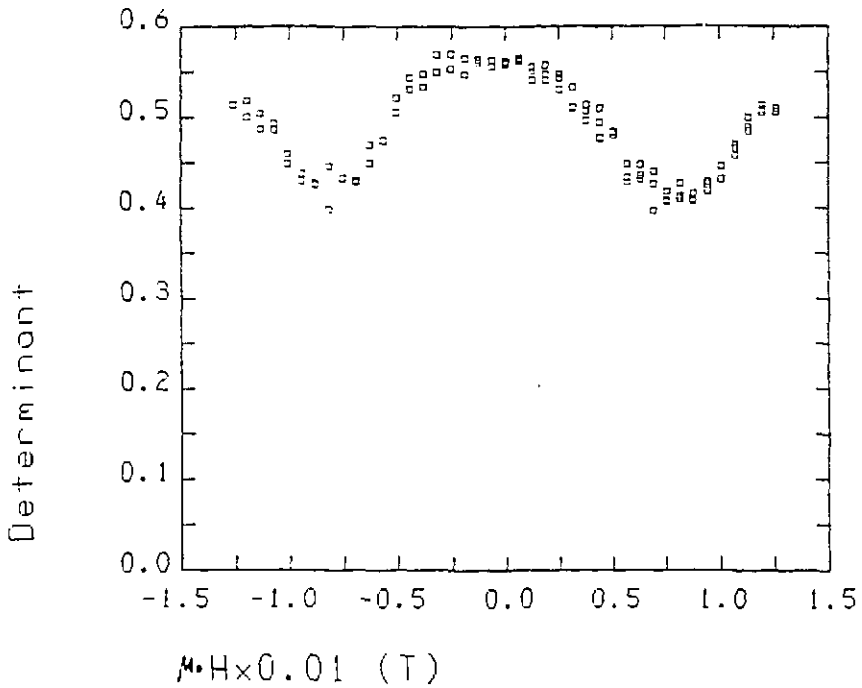

Figure 5.5 The determinant of the depolarization matrix as a function of the external field at 110 K.

5.1.2 Field cooling and zero field cooling

In the result shown in figure 5.6, the external field of 172 G is switched on at $T<T_c$ after zero field cooling (zfc). Vortices will penetrate and a non homogeneous vortex distribution can be expected, according to the Bean-model, especially at the edges of the sample. At increasing temperature more vortices will penetrate because the effective pinning force per volume f_c decreases at higher temperatures. Therefore, the external field pushes more vortices into the sample until a new stable state is reached. With increasing temperature more vortices will penetrate until at $T=T_c$ the induction in the sample is equal to the external field. The temperature is increased to 108 K to be sure that the sample is in the normal state (T_c=90.3 K). Then the sample is cooled to a temperature of 83 K in the same external field of 172 G. The field is now said to be frozen-in. It can be expected that the field in the sample is constant if the sample is field cooled to a temperature below T_c. The external field is assumed to be homogeneous and so the vortex distribution of the frozen-in field will be homogeneous. The vortex distribution in the sample will not change if it is cooled, except due to some flux creep, as there always is a balance of forces on the vortices, at any temperature. The external field which causes the force pushing the vortices into the sample, does not change so it is no

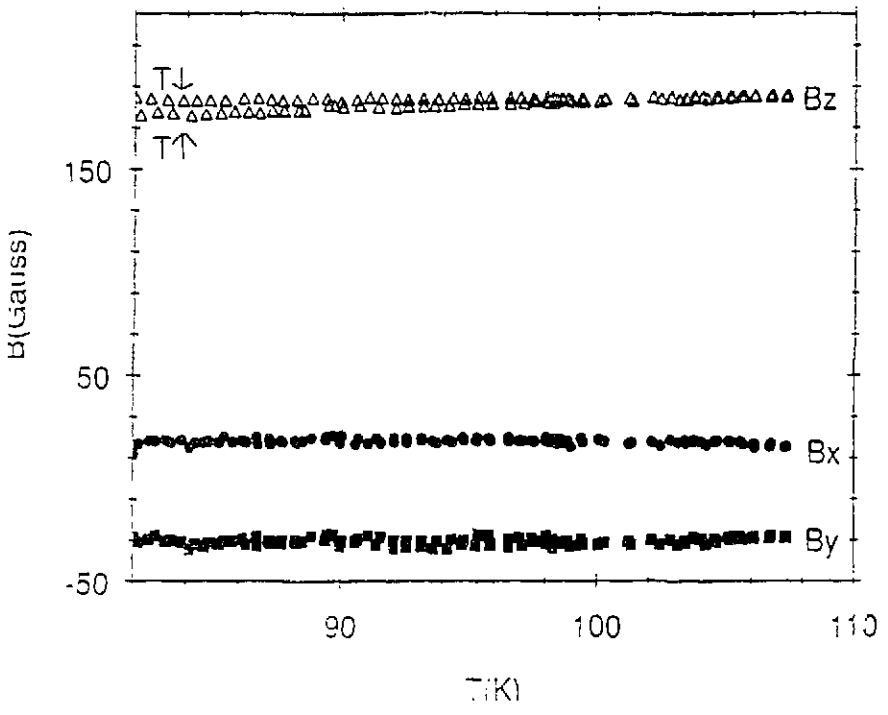

Figure 5.6 Field as a function of temperature in an external magnetic field of 172 G.

initiator for a disturbance of the balance of forces on the pinning centres. The inter-vortex repulsive forces hardly change because the distance between the centres of the vortices does not change as no more vortices penetrate the sample. So the only factor which could destabilise the system is the decrease of the vortex diameter at decreasing temperature reducing the repulsion. This sudden decrease of the vortex diameter is only an effect close to T_c and probably not measurable in this sample (see section 5.1.3). All this means that the measured magnetic field does not change if the temperature decreases. This is clearly demonstrated in figure 5.6.

The two graphs of increasing and decreasing temperature in figure 5.6 begin to differ at 101 K. this is the T_c as measured in this experiment. T_c is much higher than the literature value of 90.3 K. This difference is probably caused by a bad thermocouple, although this is checked before every measurement period.

Figure 5.7 shows $<\alpha>$ of this measurement. The depolarization is constant with decreasing temperature, this means that there is the same magnetic disorder in the sample over the neutron beam in the whole temperature range. This underlines the expectation that the vortex distribution in the sample does not change in the whole temperature range. So there will be the same distribution of flux above and below T_c while cooling, as expected.

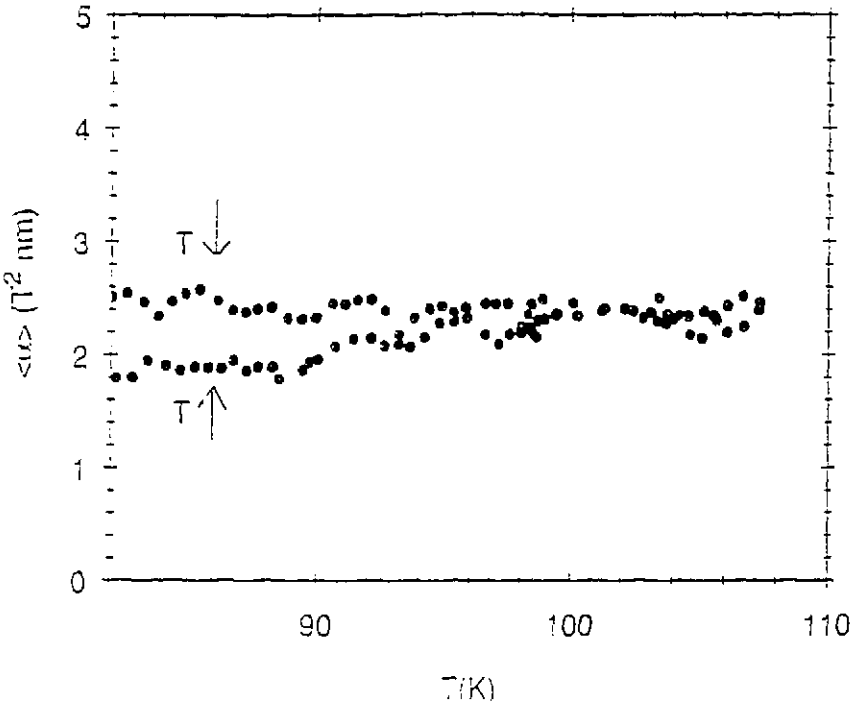

Figure 5.7 <α> as a function of the temperature.

5.1.3 Temperature dependence of the remanent state

Before the measurement was started, the sample was field cooled in an external field of 129 Gauss down to 65 K. Then, during the measurement, the temperature was increased in order to measure the remanence as a function of temperature. Because the sample was field cooled, a homogeneous distribution over the neutron beam could be assumed.

The temperature is increased to 108 K, thus much higher than T_c, to expel all vortices. A narrow diaphragm with dimensions ½ x 8 mm² is used. It is placed at 30 mm from the front of the sample. The measurement was done with the setup of figure 4.3 and 4.4 with the neutron beam transmitting the centre of the sample.

Figure 5.8 clearly shows that the z directed flux is expelled as a function of temperature. There is also some x directed flux in the sample. This perpendicular induction will be explained with help of other experiments where the effect is more obvious. The measured x directed flux stabilizes at a somewhat higher temperature than the z directed flux. At 86 K, all the flux has disappeared, except some stray field which is always present in the sample box.

The expulsion is caused by several effects. First of all by the thermal excitation of vortices out of the attractive pin potential as shown in figure 5.9. As mentioned in section 2.4 there is a Boltzmann like probability that vortices leave a pinning centre. According to Boltzmann this probability is proportional to $\exp(-U/k_BT)$. Here U is the depth of the pin potential, k_B is the Boltzmann constant and T is the temperature.

It is very likely that a vortex leaves a pinning centre of depth U if the thermal energy k_BT of the vortex is close to U. When the vortex lattice at constant temperature is stabilized, no vortices will move anymore. In that case, the thermal energy k_BT is smaller than the potential depth U of the pinning centres by which the vortices are pinned. It is assumed that if the

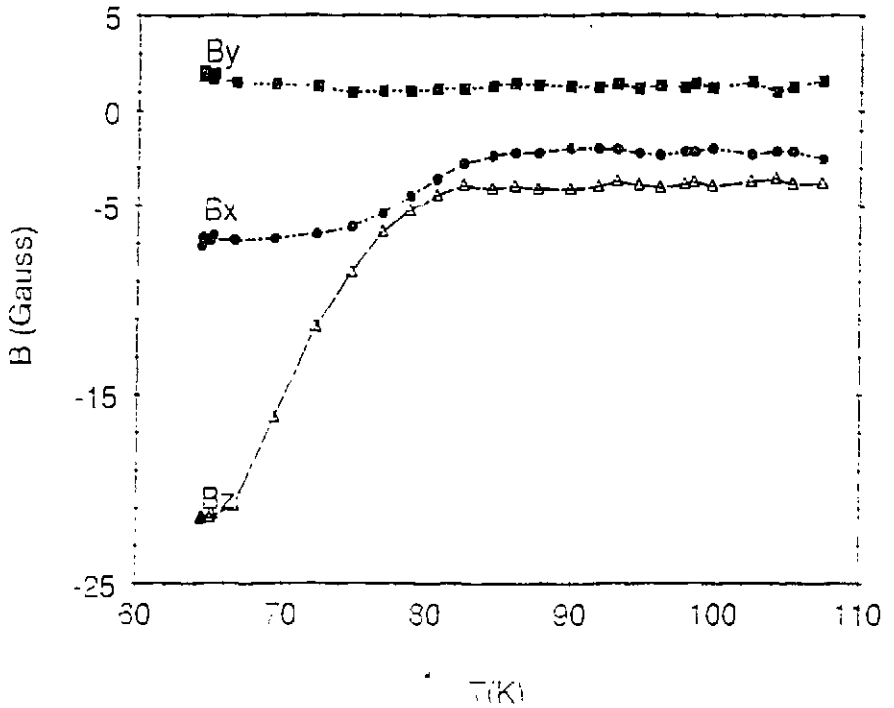

Figure 5.8 The expulsion of vortices as a result of increasing temperature. The drawn lines are a guide for the eye.

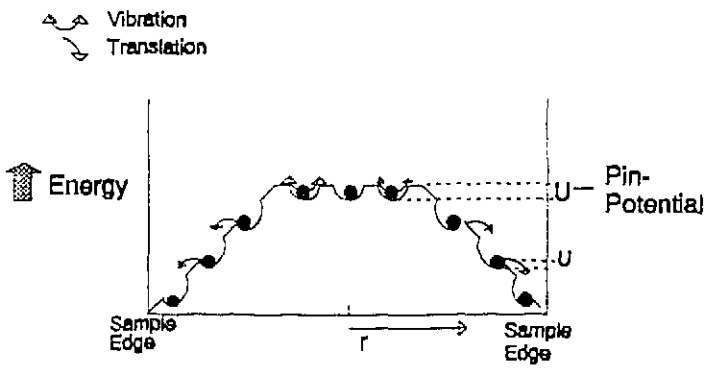

Figure 5.9 The energy profile with pin-potentials in case of remanence after field cooling, with U the depth of the potentials. The dots are vortices.

temperature of the sample increases all vortices will leave the pinning centres with a depth smaller than the new thermal energy k_BT. The new stable state will be reached almost immediatelly, as will be shown later.

Another effect causing expulsion of vortices when the temperature increases, is the decrease of the potential depth U as a function of temperature.

The effective pinning force per volume f_c will decrease because less energy and thus less force is necessary to get vortices out of the pinning centres. This decrease of f_c will cause a decrease of the gradient of the vortex distribution (see section 2.5). As the field is zero at the edge, a decreasing gradient leads to less remanence, resulting in a decrease of the magnetic field towards the edge.

It has to be mentioned that these two effects will be stronger at the edges than in the centre

of the superconductor. Because in the centre, vortices are inhibited to move as the other vortices push the vortex back in the pinning centre because of the repulsive force between the vortices which increases when the distance between the vortices gets smaller. At the edges, the vortices can move more easily because the distance between the vortices is larger (in case of a remanent frozen-in field) so that it is easier for a vortex to move between the other vortices. In other words, the vortex lattice becomed more rigid at higher densities.

A third effect leading to a lower B at higher T is the rapid increase of the penetration depth λ as a function of temperature close to T_c. In figure 5.10 this temperature dependence of λ is plotted. Although fig. 5.10 shows the effective penetration depth in $Yba_2Cu_2O_x$, a simular behaviour of the penetration depth of $Bi_2Sr_2CaCu_2O_8$ can be observed. Due to the strong increase of λ_{eff} close to T_c, the vortex diameter, which is in the order of $2\cdot\lambda_{eff}$, also increases strongly. This leads to a stronger repulsion of the vortices, because the shield current around the vortex gets closer to the magnetic field of a neighbouring vortex, resulting in a stronger

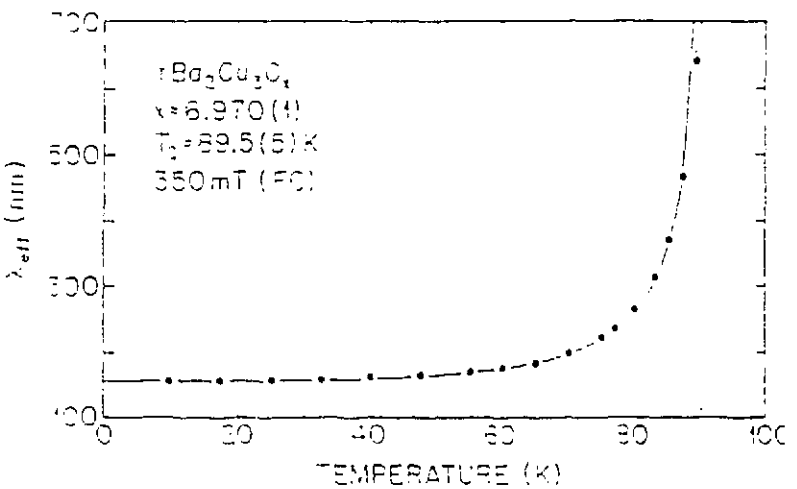

Figure 5.10 Effective penetration depth λ_{eff} as a function of temperature for a sintered $YBa_2Cu_3O_x$ in an external field of 350 mT [11]

repulsion (see section 2.3). This effect only plays an important role if the vortices are very close together (in the order of the vortex diameter) or at $T \approx T_c$ because both the field and the circular current around a vortex drop exponentially as a function of the radius of the vortex. The distance between the vortices has been calculated for the measurement shown in figure 5.8, using eq. 2.5, and has been plotted as a function of T in fig. 5.11.

Figure 5.11 makes clear that the distance between the vortices is much larger than the vortex diameter in figure 5.10, so it can be expected that this λ-effect plays almost no role.

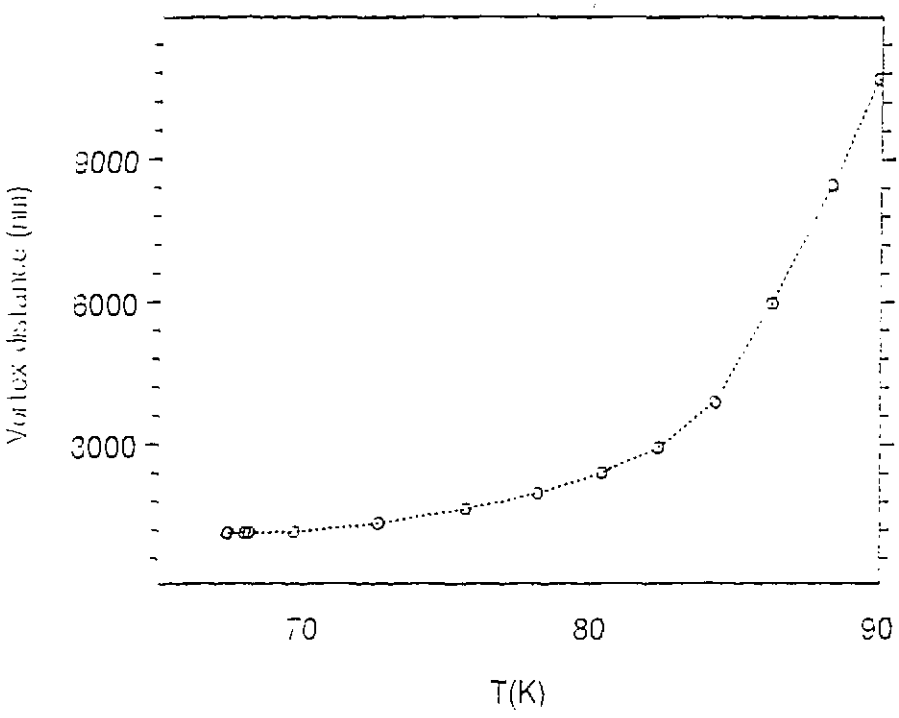

Figure 5.11 The distance between the vortices as a function of the temperature. The drawn line is a guide for the eye.

5.1.4 **Scanning after field cooling.**

To measure the vortex distribution in the sample, the sample is scanned as described in section 4.4. First a frozen-in remanent field is created by placing the sample at a temperature above T_c in an external field of -240 G. After that the temperature is brought down to 75 K and the external field is switched-off.

The measurement time at one scan angle was about 20 minutes. The smallest measurable rotation angle is 0.25° which leads to a displacement of the beam on the centre line of the sample of about 0.15 mm over the whole scan-angle range from -6° to 13°.

The temperature should not be too low, because the effective pinning force per volume f_c could then be too large and thus the gradient of the vortex distribution would be too steep to be measurable. The temperature shouldn't be too high as there would be too little remanence for ND to measure. The chosen temperature was a compromise to avoid both problems as much as possible.

Due to the divergence of the neutron beam of 0.5°, the cross-section of the beam is larger than the cross-section of the diaphragm. The centre line of the sample is situated 33 mm behind the diaphragm, resulting in a width of the neutron beam at the centre line of the sample of 0.8 mm.

Even in the case of a perfect homogeneous vortex distribution, a gradient in the distribution will be measured near the sample sides. There is a certain position range near 0 mm over which the neutron beam will not fully transmit the sample because of the sidelong entering of the sample by the neutron beam. If only a fraction of the beam transmits the sample, only a fraction of the field will be measured until the whole beam transmits the sample. In case of a homogeneous vortex distribution and a homogeneous distribution of the neutrons in the

neutron beam, which is assumed. this leads to a constant gradient as the measured field is proportional to the fraction of the beam that transmits the sample. To determine whether the gradient in the magnetic field is caused by a vortex distribution, and not just by the sidelong penetration of the neutron beam, the errors in both the position and the measured field are calculated. The minimum and maximum gradients allowed within the error bars can then be determined. If these gradients are les than infinity, a non-homogeneous vortex distribution can be concluded.

Before the measurement is started, the polarimeter is calibrated with the calibration coil mounted in the cryostat. as described in section 4.4. At large scan angles (>11°), or beyond position 6 mm. the neutron beam leaves the sample at the side instead of at the back, leading to much smaller transmission lengths. This can be corrected for.

The resolution of the position is determined by 3 factors:

1 The width of the diaphragm which partly determines the width of the beam.
2 The divergence of the neutron beam making the beam wider than the diaphragm.
3 Oblique transmission: the positions at which the beam enters and leaves the sample are not equal.

All these factors lead to an uncertainty in the position at which the field was measured. The resolution at position 0 mm is the highest because here the beam enters the sample perpendicular to the surface. The resolution near 0 mm is only determined by the width of the neutron beam and the divergence of the beam.

Figure 5.12 shows the remanent field as a function of the position on the centre line corrected for different transmission lengths.

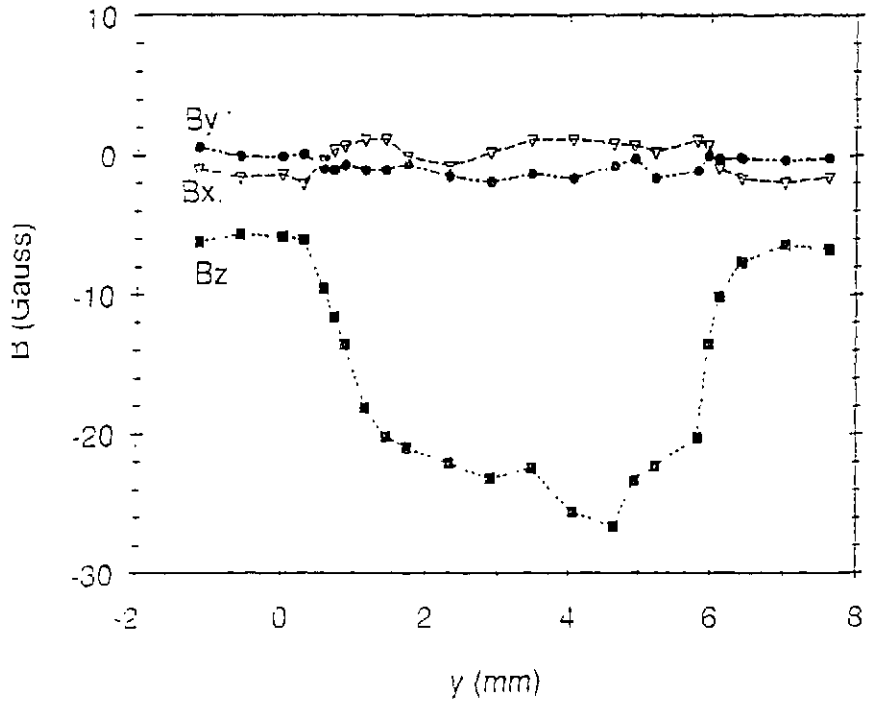

Figure 5.12 Remanent field as a function of position. The drawn line is a guide for the eye.

Although there still is a small x field, it is much smaller than the x field of the measurements discussed before due to a much better calibration. Outside the sample an external z field of

about -5.5 Gauss is measured. This field is due to a non perfect calibration and stray field. There is also some x and y field in the range between -1 Gauss and 1 Gauss. In the position range from 0 mm to 6 mm, the z remanence is clearly visible. Between 4 mm and 5 mm there is a peak in the z remanence. This dip is probable due to a bad region with more pinning centres where the sample is able to hold more vortices.

There is a gradient in the z remanence at the sides, although from figure 5.12 it is not clear whether this is a gradient due to a vortex distribution or only due to the sidelong penetration

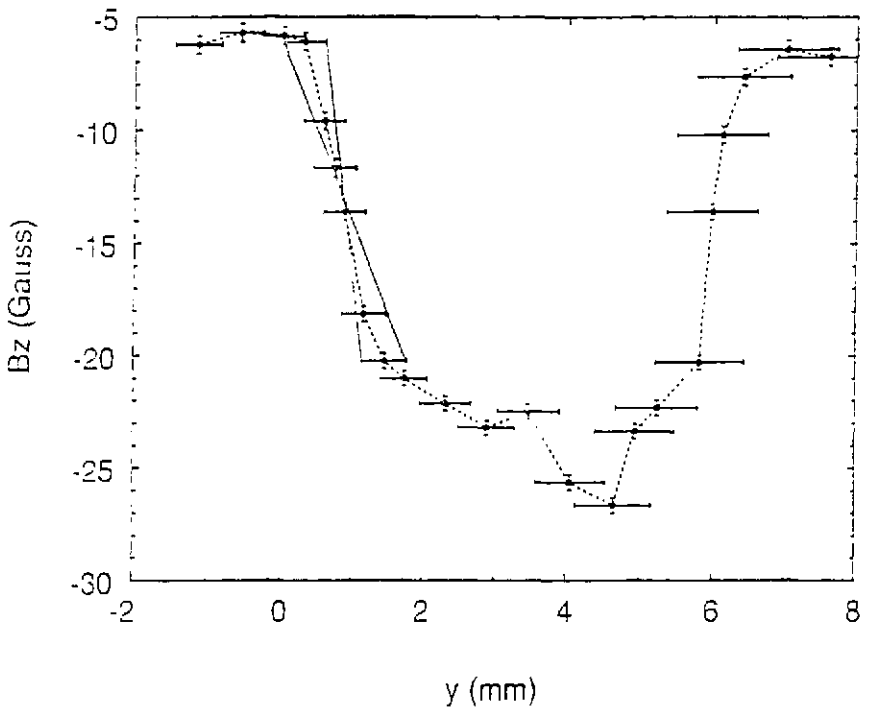

Figure 5.13 Z-remanence as a function of the position.

of the neutron beam. Figure 5.13 shows the z remanence including its error bars. The two lines are the maximum and minimum gradients within the error bars. Figure 5.13 makes clear that there is a gradient of the vortex distribution as the steepest gradient allowed within the error bars is smaller than infinity. The minimum gradient is -8.03 Gauss/mm, the maximum gradient is -25.7 Gauss/mm, and so the average gradient -16.87 Gauss/mm. With help of eq. (2.10) the average critical current density j_{ca} for flux flow, according to the Bean-model, can be calculated: $j_{ca}=1.3\times10^{6}$ [A m^{-2}]. The y-error bars increase considerably at large positions because the effect of oblique transmission of the beam at these positions increases rapidly.

The remanence is assumed constant in time during the whole scan measurement. In another measurement, which is not shown, a change in the remanence could not be observed even after seven hours of measuring with much better statistics. Apparently the vortices are very strongly pinned. Not only the pinning centres inhibit the vortices to move, but also the vortex lattice, because the lattice has to be deformed if a vortex moves through it.

5.1.5 Scanning in constant field after zero field cooling

In this measurement the sample is scanned at a temperature of 75 K and in an external field of -98 G. Again the system is calibrated before the measurement, with the calibration coil mounted in the cryostat.

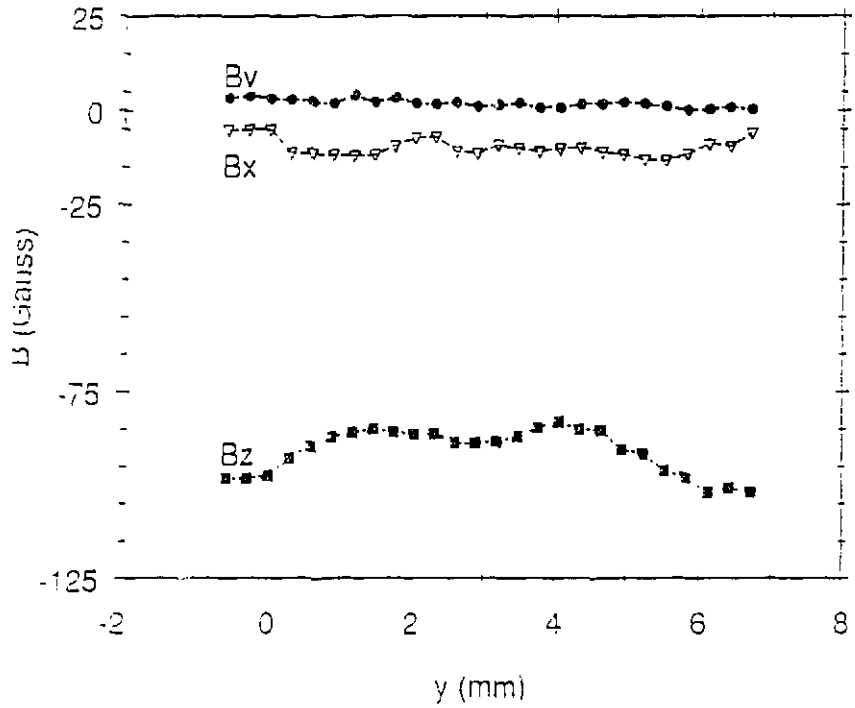

Figure 5.14 Scan in a constant field of -98 G at 75 K after zero field cooling

From figure 5.14 it becomes clear that the x and y fields are small compared to the z field, as expected although still a position dependence of the x field is observed. There is a non homogeneous distribution in the z-field near the sides. To find out whether the gradient at the sides is only caused by the entering of the beam or also by the vortex distribution, the method in section 5.1.4 is used. Again the x-error bars are results of the divergence of the beam, the width of the diaphragm and the oblique transmission of the beam. The z field is corrected for different transmission lengths at different positions. Figure 5.15 shows the z field with error bars and the gradients allowed within the error bars.

Again the maximum gradient allowed within the error bars is less than infinity, and so there is a measurable gradient in the vortex distribution. The maximum gradient within the error bars is 39.4 Gauss/mm and the minimum gradient is 7.3 Gauss/mm and so the average gradient is 23.35 Gauss/mm hence j_{ca}=1.86x10^6 [A m^{-2}].

There is a dip in the z field in the centre of the sample, which means a stronger field because the external field is negative. Maybe at this position the neutron beam transmits a part of the sample with less pinning centra that can more easily be penetrated by vortices.

A symmetric vortex distribution can be expected if all other factors like the external field and the properties of the sample are symmetric. However there is less penetration in the position range between 4 mm and 5 mm than in the position range between 1 mm and 2 mm. This is again an indication that the effective pinning force per volume f_c is larger in the region between 4 mm and 5 mm than in the region between 1 mm and 2 mm. It is apparently

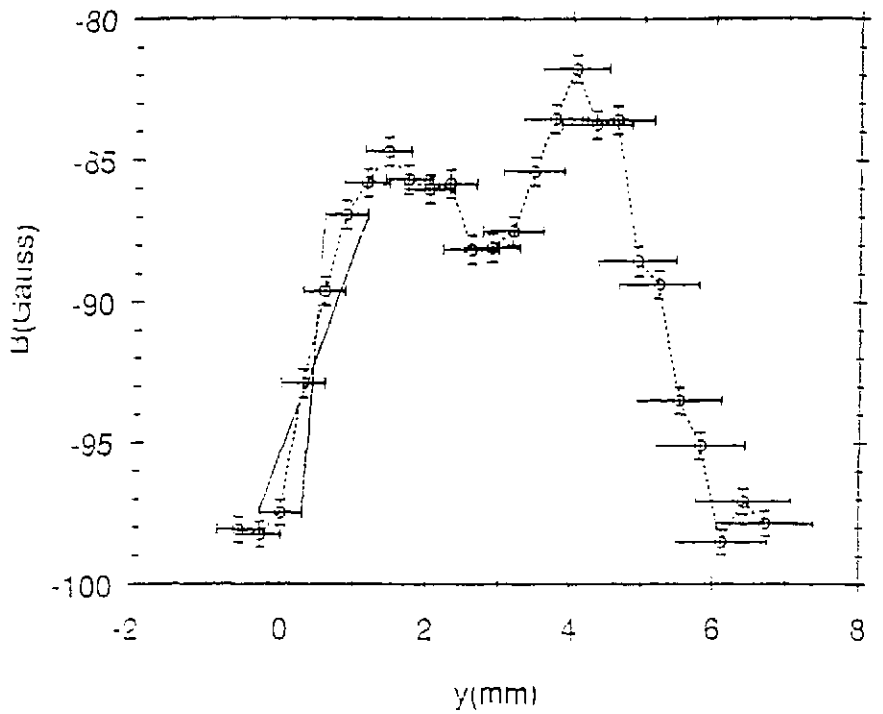

Figure 5.15 z component of the magnetic field with error bars

more difficult for the field to penetrate the second region.

5.2 Pulse measurements

In the experiments described in this section, the remanence after a pulse is measured as a function of position, as a function of time, as a function of temperature and as a function of the maximum field in the pulse.

5.2.1 Scanning after zero field cooling and a field pulse

The results shown in figure 5.16 are the calculated fields of two measurements combined. In the first measurement the sample temperature is brought to 75 K in zero field after which a magnetic field pulse of 1.6 T (16 kG) and a duration of 1 ms is applied. Then during 12 hours a scan between -1 mm and 7.6 mm is made. In the second measurement a field pulse of 2.1 T with a time duration of 1 ms is applied at a temperature of 69 K. The magnetic field is measured at positions outside the sample, $-4\ \text{mm} < y < -.5\ \text{mm}$.

The remanent field is expected to be in the same direction as the external field. Figure 5.16 shows a completely unexpected effect. A large field pulse in the z direction causes x and y fields of a magnitude larger than the magnitude of the remanent z field. The x and y fields have field-maxima that are positioned rather symmetrical around the centre of the sample. The z field also has maxima though they are not symmetrical. All fields have their first maximum near position 1.5 mm. As the external field is in the z direction, the result of this measurement implies that vortices will redirect in the x and y direction after the pulse has ended. It is assumed that vortices or parts of vortices that have redirected, are situated in the xy-plane, as shown in figure 5.17 in which only the y redirected vortices are shown. This redirection

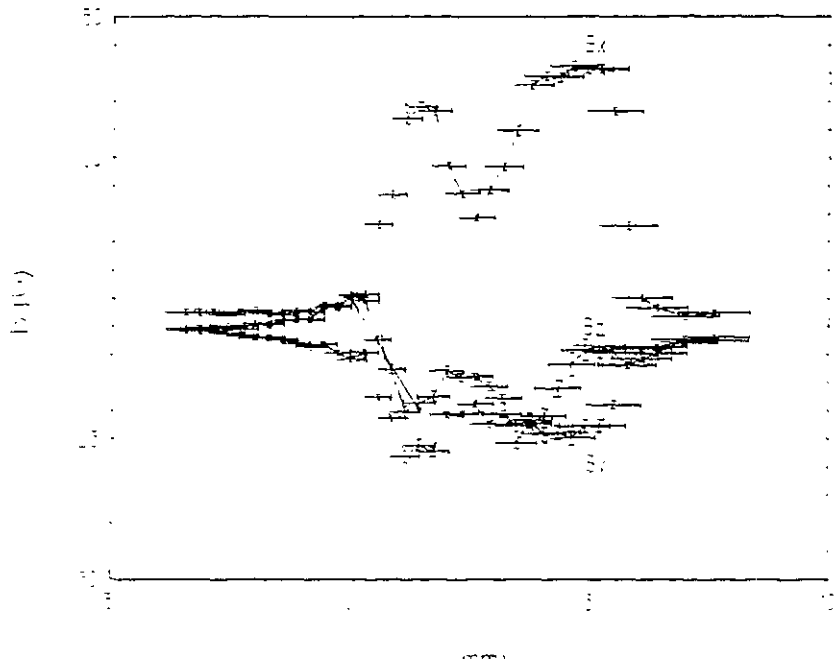

Figure 5.16 Remanence after pulse. The remanence in the sample is caused by a pulse of 1.6 T at 75 K. The remanence outside the sample is caused by a pulse of 2.1 T at 69 K.

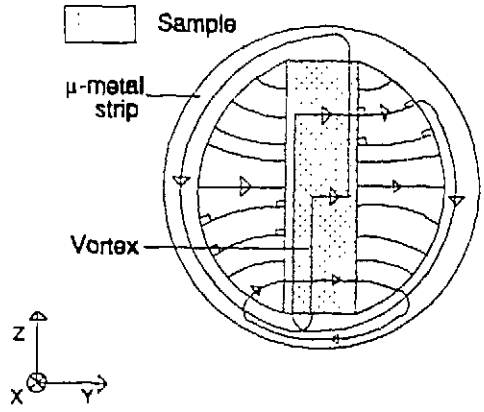

Figure 5.17 Vortices after redirection. The field outside the sample is perpendicular to the surface of the sample and the μ-metal strip.

of vortices is explained in section 5.2.5. The flux of some vortices that have redirected, leaves the sample at the sides. This flux causes the y and z fields outside the sample. Because these vortices are in the xy-plane, the flux of these vortices leaves the sample parallel to the normal axes of the sample surface. The remanence between 4 mm and 5 mm is again larger than the remanence between 1 mm and 2 mm, again one can conclude from this, the probable larger effective pinning force in that region.

The maximum and minimum gradients within the error bars of the z field near the side at 0 mm, are calculated and plotted in figure 5.16. The gradient in the z field is smaller than infinity so a gradient in the vortex distribution can be concluded. The maximum gradient is

-80.5 Gauss/mm and the minimum gradient is -13.5 Gauss/mm. The average gradient is 47 Gauss/mm and so the average critical current density is 3.6×10^6 [A m^{-2}]

In fig. 5.18, $\langle\alpha\rangle$ is plotted as a function of position. In the sample $\langle\alpha\rangle$ fluctuates considerably. At the positions of high gradients (near the sides and at 3.5 mm) $\langle\alpha\rangle$ is large because of the inhomogeneous field distribution over the neutron beam at the positions with a field gradient. At position 5 mm all three fields are quite constant. At this position $\langle\alpha\rangle$ is close to 2×10^{-9}, which means a small depolarization (~1%), according to eq.(3.14). As there is almost no fluctuation of the magnetic field at this position, depolarization can only be caused by correlations of vortices smaller than the beam width. When we assume that $\langle\alpha\rangle \sim 1 \times 10^{-9}$, then this corresponds to a correlation length of 0.2 mm of the measured magnetic induction of 50 Gauss. This correlation length is in the order of the thickness of the crystallite platelets (~0.1 mm).

Outside the sample $\langle\alpha\rangle$, and thus the depolarization, increases. This can be explained as follows: As the flux follows the shortest route towards the μ-metal strip, it will be perpendicular to the circularly wrapped μ-metal strip, which results in many different flux directions over the neutron beam near the μ-metal strip. These many different directions result in more depolarization the closer the scanning neutron beam approaches the μ-metal strip. See figure 5.17.

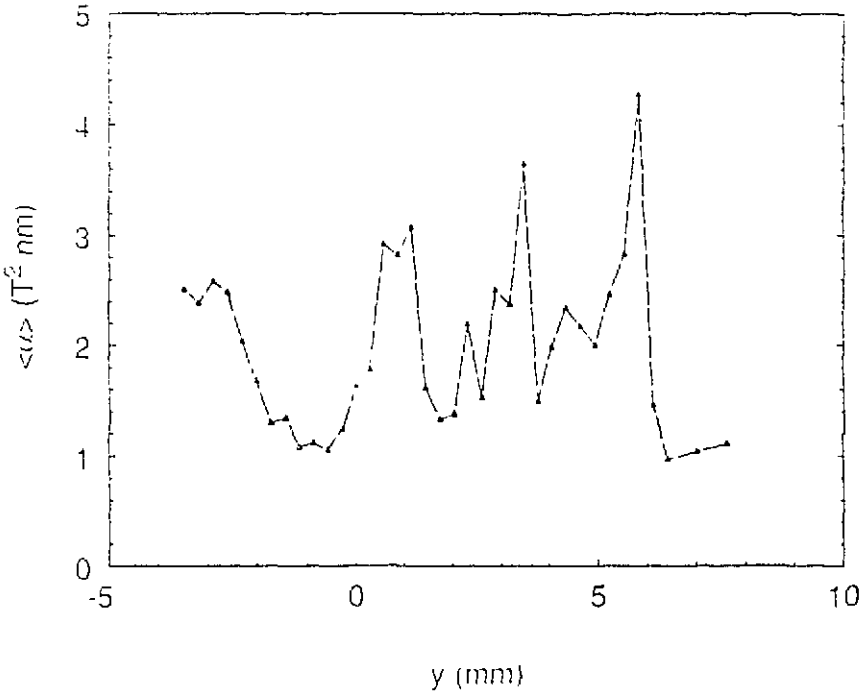

Figure 5.18 $\langle\alpha\rangle$ as a function of the position on the centre line of the sample. The drawn line is a guide for the eye.

To learn more about the unexpected x and y fields, the development of these fields needs to be studied as a function of time, as a function of temperature and as a function of the maximum field of a magnetic pulse.

5.2.2 Dynamic measurements

With dynamic measurements the magnetic behaviour of the sample is studied as a function of time. In the measurements, the sample is studied during 500 ms, in which a pulse of 1 ms was applied. A narrow diaphragm of ½ x 8 mm^2 is used to measure the dynamic behaviour of the sample at different positions in the sample. These positions were 1.5 mm, 3 mm and 4.5 mm, this is in the centre of the sample and at the two field maxima (1.5 mm and 4.5 mm) resp. of the measurement shown in figure 5.16. The measurements at position 1.5 mm and at 4.5 mm are started 20 msec before the pulse, the measurement in the centre is started at the time of the pulse. During these 500 ms, 500 depolarization matrices were measured, so every matrix represents 1 msec. As there are only 600 monitor counts in the narrow neutron beam, many pulses have to be generated to accumulate enough neutrons per depolarization matrix to obtain reasonable statistics. For that reason, one dynamic measurement takes about 24 hours.

In the dynamic measurements, a pulse generator was used to apply field pulses of 2 T, at a rate of two per second. Due to heating by the Ohmic losses in the coil, the sample temperature would increase from 65 K, the temperature of the pumped nitrogen bath, to about 71 K. To avoid this temperature effect while pulsing, the temperature is first brought to 71 K using the heating wire. The measurement is started after stabilization of the temperature.

Figures 5.19, 5.20 and 5.21 show the magnetic field in the first 500 ms after the pulse, at positions 1.5, 3 and 4.5 mm respectively.

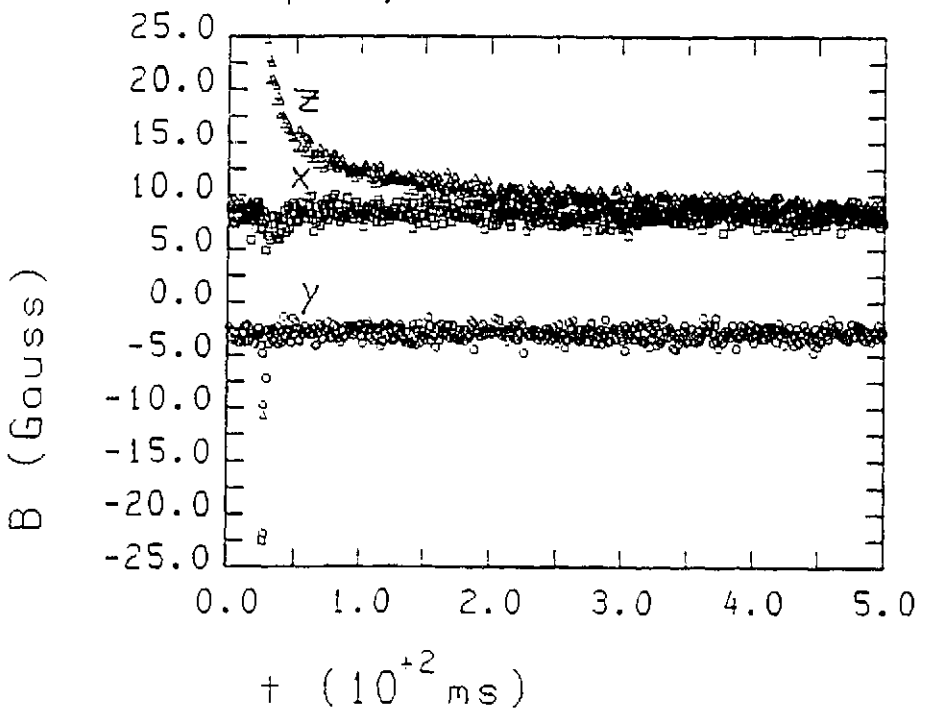

Figure 5.19 The field after pulses of 2 T at 71 K at position 1.5 mm. The squares, circles and triangles indicate the x-, y- and z- field resp.

Right after the pulse the z field is large as the pulse is z directed. Because a magnetic field has a positive energy per volume, called the field energy, the vortices lower their volume by straightning and align. So during the pulse there will only be z directed flux.

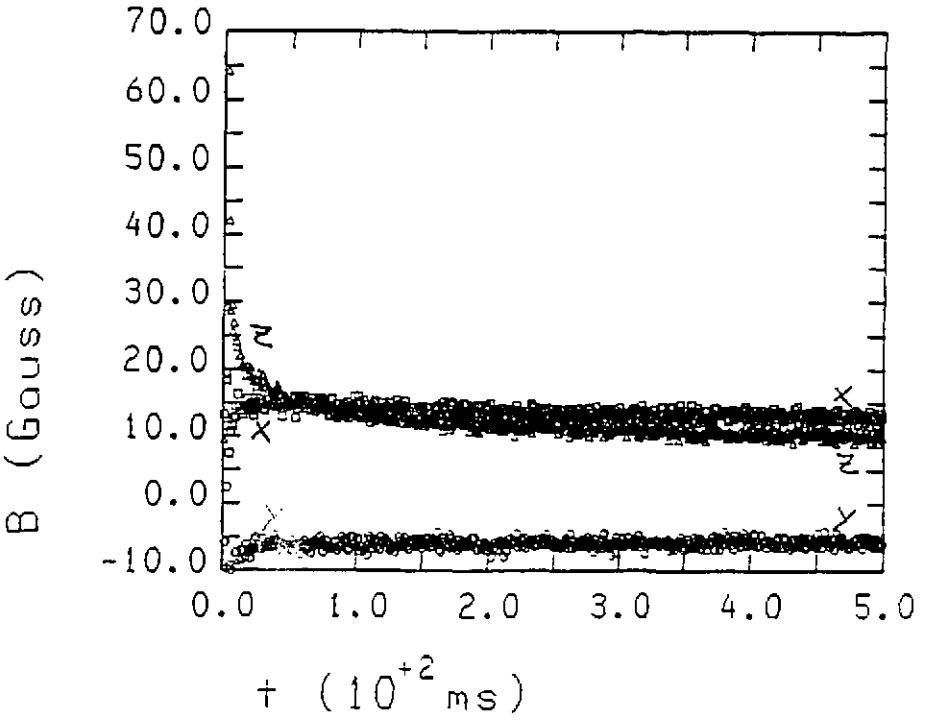

Figure 5.20 The field after pulses of 2 T at 71 K at position 3 mm. The x-,y- and z- field is indicated with the squares, the circles and the triangles resp.

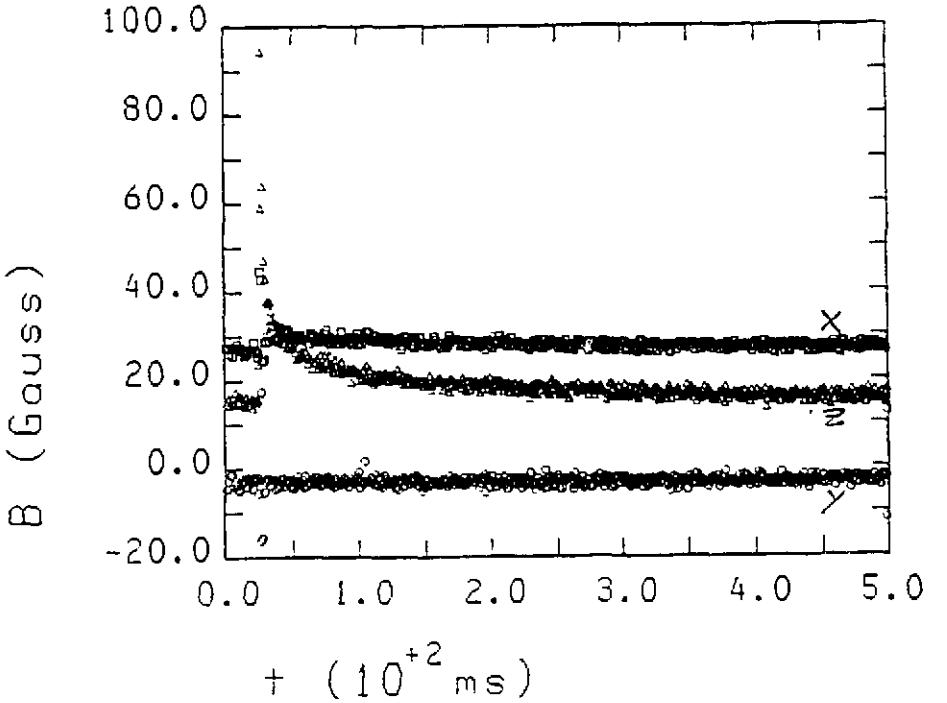

Figure 5.21 The the field after pulses of 2 T at 71 K at position 4.5 mm. The sqaures,circles and triangles indicate the x-, y- and z-field resp.

In the field pulse, many vortices will be forced to penetrate the superconductor. Because of this large penetration, all pinning centres will be occupied with vortices resulting in a decrease of the attractive force on the vortices by the pinning centres due to the repulsion of a vortex by other vortices pinned in the pinning centre. It can also be said that due to the large density of vortices right after the pulse, the effective pin potential becomes less deep. After the field

pulse, in zero external field, vortices will be expelled from the superconductor because of the repulsive force between the vortices which is strong, as the vortices are packed closely together. The expulsion is mainly due to the expansion of the closely packed vortices right after the pulse. The expansion of the vortex lattice leads to a collective movement of the vortices and is happening on a relatively short time scale. After some time the most weakly pinned vortices will have left the superconductor. Then the expulsion of vortices is dominated by flux creep, due to thermal excitation of vortices out of their pinning centres. This expulsion takes place on a much longer time scale because the pinning centres are more able to inhibit the vortices to move.

To show that the expulsion of vortices is not only caused by thermal excitation, the z field is fitted to equation (5.1) [12], which describes expulsion due to flux creep.

$$|B| = a*(1-b*\ln(1+t/\tau)) \tag{5.1}$$

y (mm)	a (Gauss)	b	τ (ms)
1.5	23.27	0.096	0.60
3.0	26.82	0.103	1
4.5	44.12	0.084	0.20

Figures 5.22, 5.23 and 5.24 show that equation 5.1 does not properly describe the behaviour of the remanence right after the pulse. So indeed not only flux creep plays a role in the expulsion of flux.

Because the magnetic field after the pulse is not parallel to the main axes, $<\alpha>$ has to be calculated. The figures 5.25, 5.26 and 5.27 show $<\alpha>$ as a function of time. At y=1.5 mm and y=3 mm, a decrease of $<\alpha>$ as a function of time is observed. The expulsion of vortices right after the pulse is apparently a very chaotic proces. At y=4.5 mm $<\alpha>$ is smaller than 2×10^{-9}, except during the first 10 ms after the pulse. This small $<\alpha>$ means that the expulsion of flux is a rather orderly proces at position 4.5 mm.

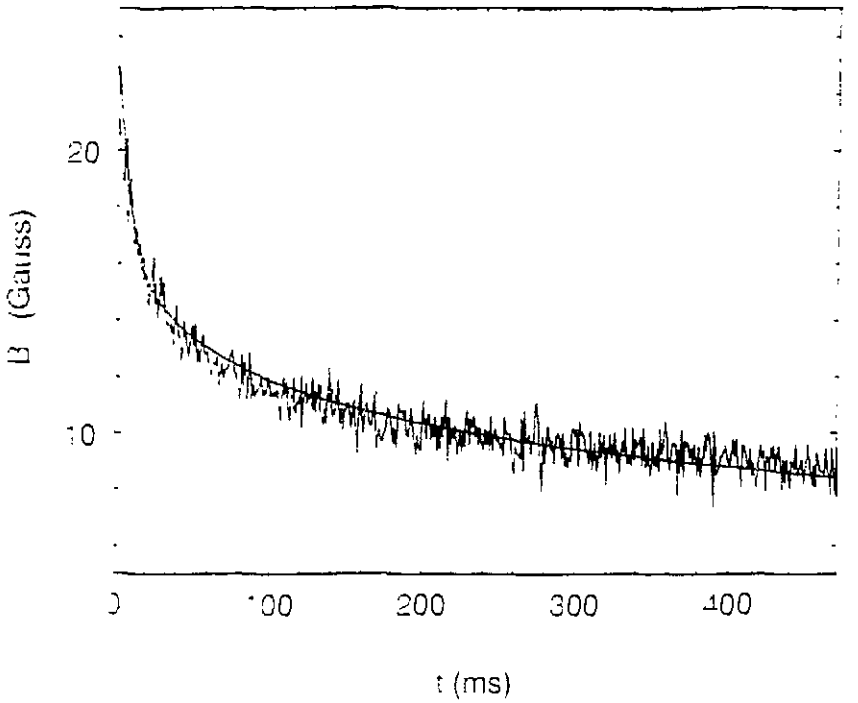

Figure 5.22 The expulsion of flux, 500 ms after the pulse at 1.5 mm and a fit (drawn line) of expulsion only due to flux creep

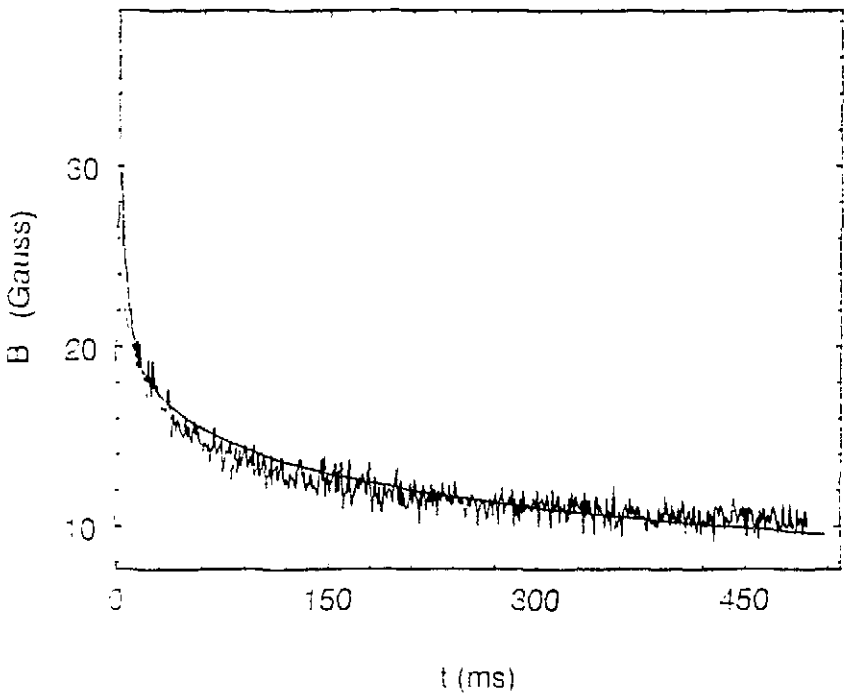

Figure 5.23 The expulsion of flux 500 ms after the pulse at 3 mm and a fit (drawn line) of expulsion only due to flux creep

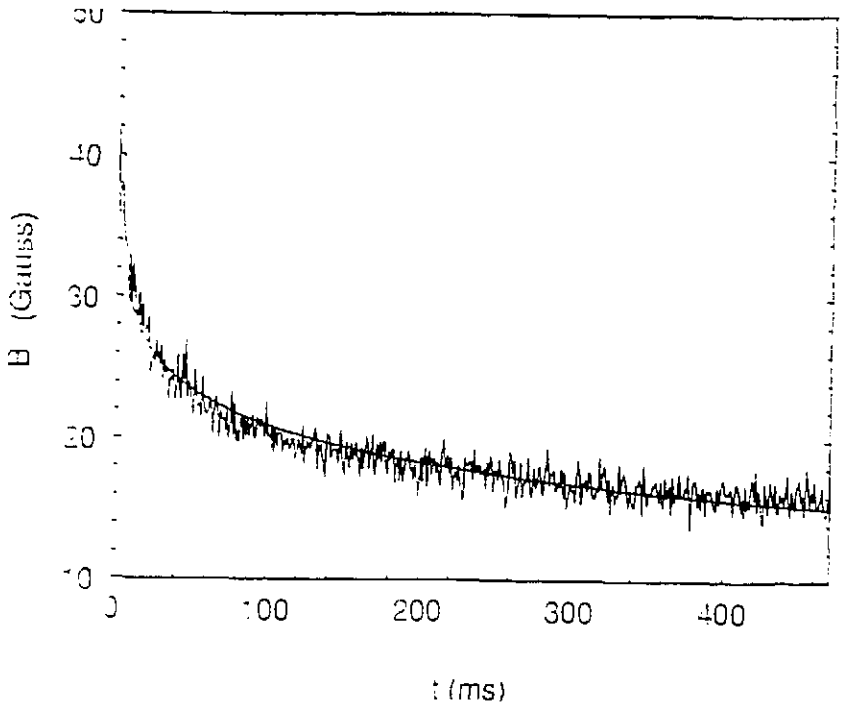

Figure 5.24 The expulsion of flux 500 ms after the pulse at 4.5 mm and a fit (drawn line) of expulsion only due to flux creep

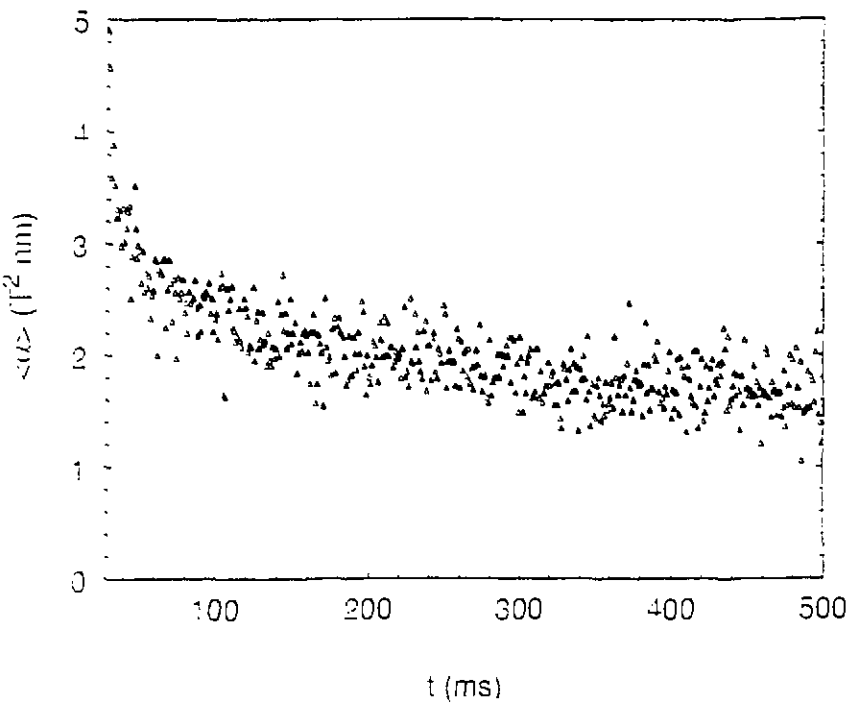

Figure 5.25 <α> as a function of time at 1.5 mm

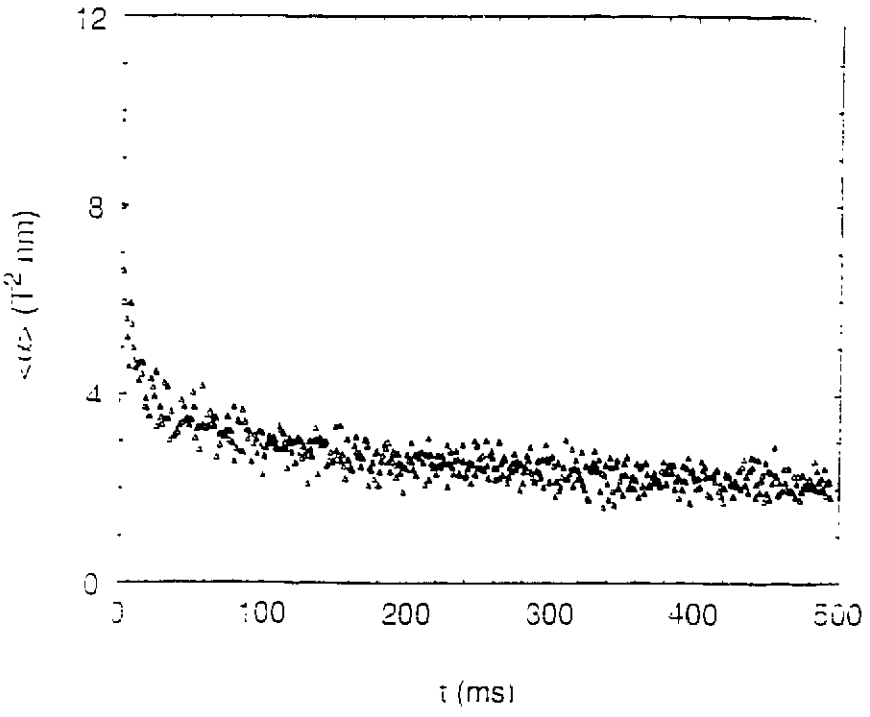

Figure 5.26 <α> as a function of time at 3 mm

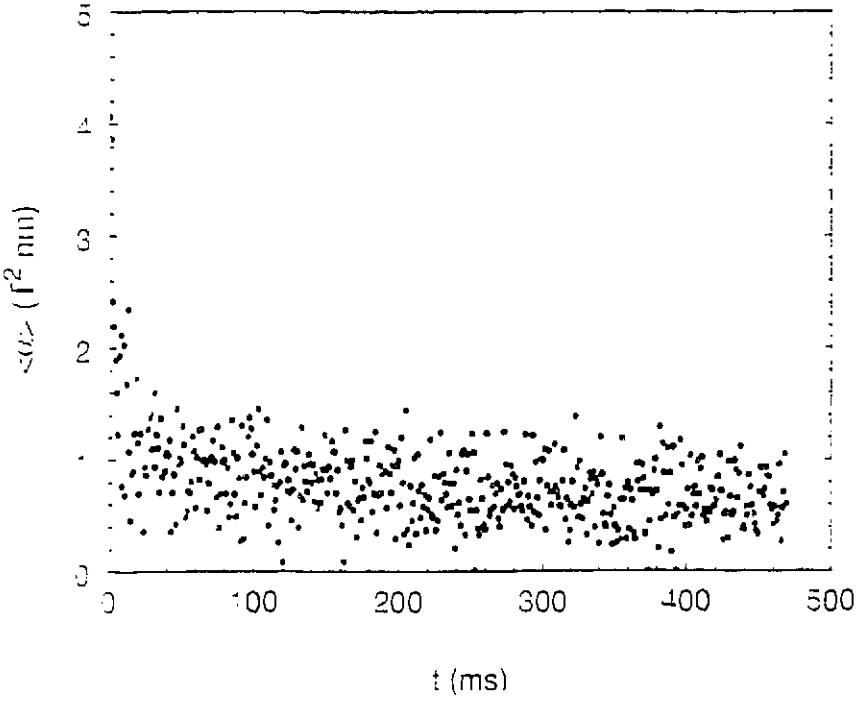

Figure 5.27 <α> as a function of time at 4.5 mm

5.2.3 Temperature dependence of the x, y and z directed flux after zfc. and a pulse

Before a matrix is measured, a z directed field pulse of 1.6 T with a duration of 1 ms is applied. The measurement is started at a temperature of 94 K. During the measurement the temperature is linearly decreased from 94 K to 78 K. The depolarization is measured with the narrow neutron beam of 0.5x8 mm^2 transmitting the centre of the sample during every 2.5 K

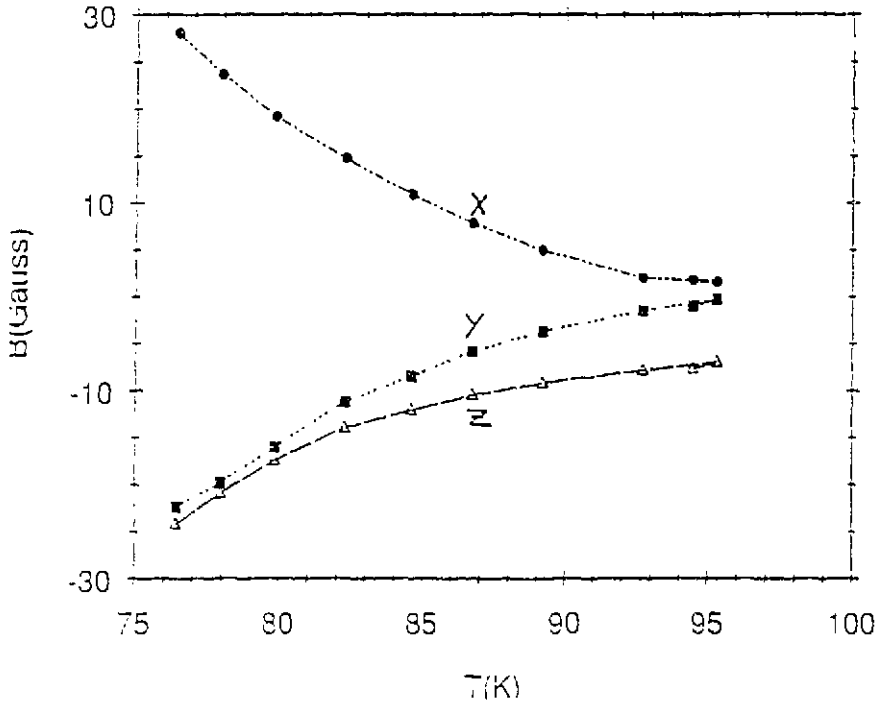

Figure 5.28 Temperature dependence of the remanence after pulses of 1.6 T before every matrix.

temperature step. Figure 5.28 shows the x, y and z field as a function of the temperature. At 94 K only the stray field is measured. At 89 K the magnitude of the field components starts to increase. The magnitudes of x and y are almost equal over the whole temperature range. The scan measurement after a pulse, figure 5.16, also showed that in the centre the x and y fields are almost equal in absolute value. Figure 5.28 shows that this is the case at all temperatures between 89 K and 78 K.

The measured remanence is clearly not proportional to the temperature. If the temperature decreases, the growth of the magnitude of the x and y field is larger than the growth of the magnitude of the z field. From this we can conclude that a larger fraction of the vortices are being rotated to the x and y direction at lower temperatures

In figure 5.29 $<\alpha>$ is plotted and shows an increase if the temperature decreases from 90 K to 80 K. This increase of $<\alpha>$ can be due to the larger remanence that makes larger fluctuations of the induction more likely, or to the increase of gradient of the vortex distribution in the centre. If the depolarization is due to the gradient of the vortex distribution, one can conclude that the gradient is not constant but increases at decreasing temperatures. This could be expected as the critical current density for fluxflow j_c increases at decreasing

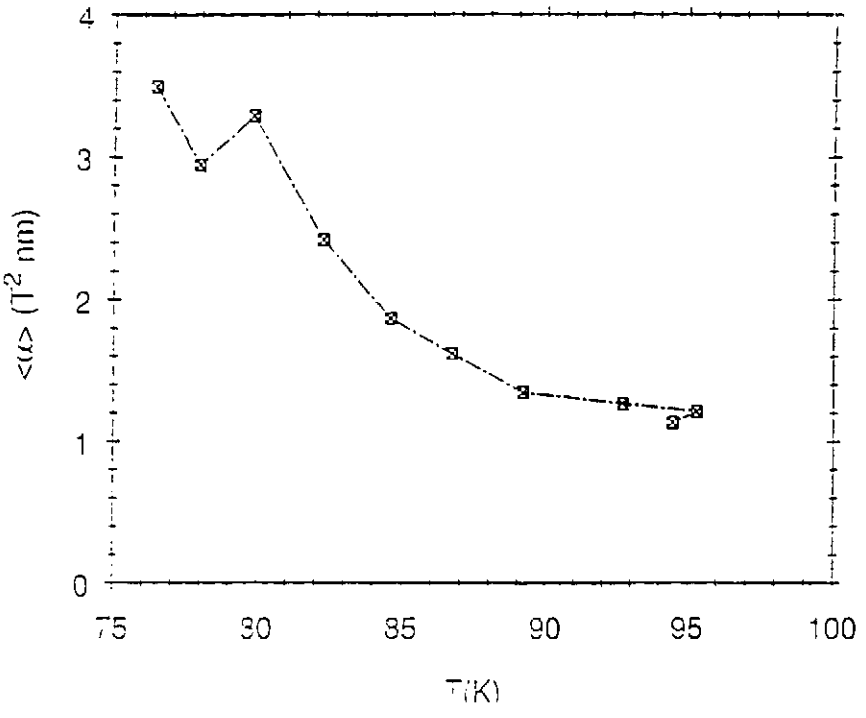

Figure 5.29 <α> as a function of temperature.

temperatures. An increase of j_c leads to a steeper gradient and thus to more magnetic fluctuation over the neutron beam when the neutron beam transmits a position with a field gradient.

5.2.4 Pulse field dependence of the remanence

To investigate the remanence as a function of increasing magnetic fields (Teslas), the field is increased and pulsed before every measured depolarization matrix. The peak value of the magnetic field pulse is increased from 0.75 T to 3.3 T at 69 K. The pulse width was 1 ms. Unfortunately smaller pulses could not be generated in this experiment because of technical limitations by the pulse apparatus that was used. After every pulse, a depolarization matrix is measured. Again the diaphragm was 0.5x8 mm^2 and the neutron beam transmitted the centre of the sample.

In figure 5.30 one can see that the x and y fields are almost equal at every point in the measured field range. This was expected from the measurements discussed in section 5.2.3 and 5.2.1, which also showed this equality of the x and y field in the sample centre. The x and y field increase to 25 Gauss and -28 Gauss resp. At pulse heigths of 3.3 T, the x and y fields reach a saturation level. To verify this, larger pulses are necessary. However larger pulses could not be generated because of the risk of melting of the coil.

The z field increases rapidly after the first few pulses. At higher applied fields, a slow decay as a function of time is observed. As the x and y fields still increase in the pulse region between above 1.4 T, one can conclude that the bending of the vortices is a faster process then the expulsion of z directed flux after a pulse. In figure 5.31 <α> increases almost linearly with field to 5 x 10^{-8} [T^2 m]. The chaos in the vortex system increases, probably because at low fields, the critical state is not yet reached as can be seen from fig. 5.30.

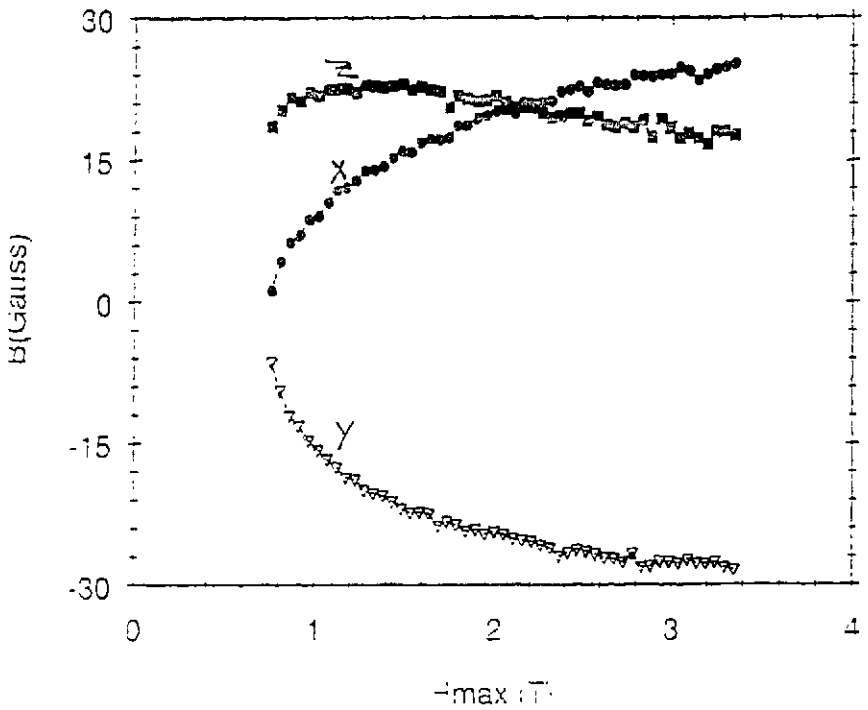

Figure 5.30 Remanence as a function of the maximum field in the pulse at 69 K.

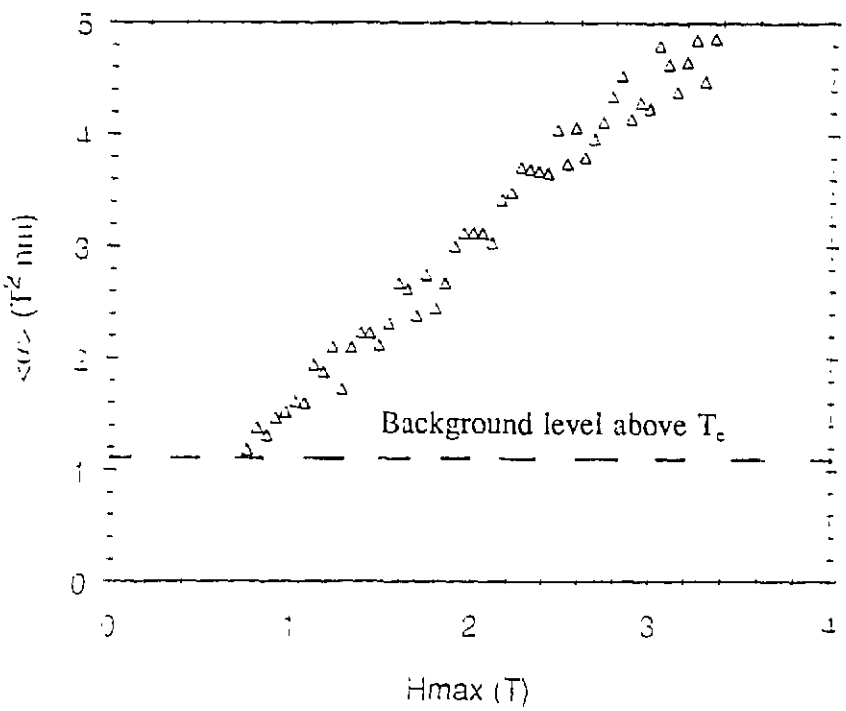

Figure 5.31 <α> as a function of the maximum field in the pulse

Therefore the gradients can still increase with higher applied field. It is also possible that the redirection of vortices, necessary to establish these large x and y fields, is a very disorderly process so that there are large fluctuations of x and y directed flux over the neutron beam.

6 Discussion of strong x and y fields

As explained in chapter 4, the sample consists of crystallite platelets of the Bi(2212) lattice structure. The c axes, which are perpendicular to the CuO planes, are all in the xy-plane and randomly distributed. In the CuO planes large currents of Cooper pairs, called super currents, are possible. Much weaker tunneling currents are possible in planes perpendicular to the CuO planes. An explanation for the source of the supercurrents is not known yet and is not essential to understand the following.

The planes between the crystallite platelets are weakly superconducting, which has two important consequences:

1 The planes between the crystallites are less able to expel the external field, and so vortices will easily penetrate these planes.

2 Because these planes are weakly superconducting, they are closer to the normal state, like pinning centres that are normal or almost normal spots in the superconductor. As a consequence they act as pinning planes that attract vortices.

To be able to explain the x and y fields, a small angle β between the z field and the crystallite platelets, and thus the CuO planes, is assumed (see figure 6.1).

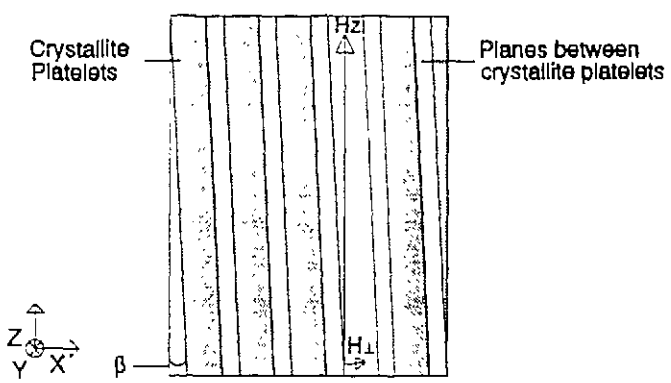

Figure 6.1 The perpendicular field component $H_{\perp}$ in an external field Hz

Due to this small angle β there will be an external field component $H_{\perp}$ perpendicular to the crystallite planes. At a certain external field, $H_{\perp}$ along the c axis exceeds a critical perpendicular field $H_{\perp c1}$. If $H_{\perp c1}$ is exceeded, vortices can penetrate parallel to the c axis. In the high field of a pulse, all vortices will be directed parallel to the applied field, in order to obtain the lowest field energy. After a pulse, most vortices will be expelled from the superconductor because during the pulse, the field in the superconductor is much higher than the remanent saturation field. However some vortices will be pinned. Some of these vortices will partly be in the crystallite platelets. The circular currents around the vortices in the crystallite platelets, tend to flow in the CuO planes, because these planes are strong superconducting.

A circular current in a CuO plane is a small magnetic dipole, that attracts the dipoles caused by the circular currents in the neighbouring CuO plane (see figure 6.2). Because of this attractive force, the dipoles want to move closer together. If this happens, the vortex in the crystallite rotates to a direction parallel to the c-axis. This rotation of the vortex causes small local x and y fields. These x and y fields would not be measurable because an x or y field due to a rotated part of a vortex in the crystallite platelets is compensated by an opposite x

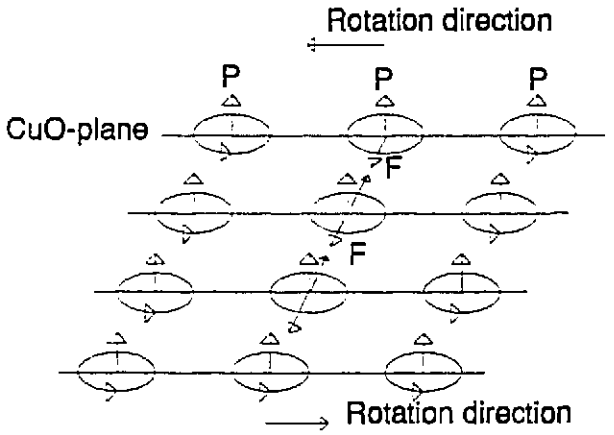

Figure 6.2 Rotation of vortices in the crystallite platelets due to the attractive force **F** between the dipole moments **P** in the CuO-planes

or y field component due to the mainly z directed part of the same vortex between the crystallite platelets. So also another event has to play after the pulse in order to create large x and y fields.

It is possible that vortices, despite the repulsive force between the vortices, combine in a special way. If the bending points of bundles of vortices overlap, the x or y parts of the vortices could combine as well as the z parts, because the z directed magnetic dipole moments of the vortices of both bundles attract each other, as well as the x or y directed magnetic dipole moments. If this force is larger then the repulsive force between the vortices, the x or y parts and the z parts of the bundles of vortices combine. After that the new and z directed vortices are expelled, because these vortices are situated between the crystallite platelets which have a low saturation level due to the weak superconductivity in these planes. More x and y flux will be left. This combining of vortices occurs in the first few milli seconds after the pulse, because during that time the sample is filled with many vortices which makes it more likely for vortices to be pact together between the crystallite platelets. So during that time the x and y fields have to be formed. This is observed in the dynamic measurements.

The reason for the decrease of the z remanence at increasing pulse fields is the larger probability for the cross-over of vortices i.e. the perpendicular penetration of vortices, resulting in more x and y flux between the crystallite platelets breaking some Cooper pairs and thus decreasing the saturation remanence for the z directed vortices.

7 Conclusion

The scan measurement of both the vortex distribution after zero field cooling in an external field and the vortex distribution of the remanence after field cooling showed the presence of a gradient in the vortex distribution. Thus a non homogeneous vortex distribution can be concluded. Due to the width of the neutron beam at the sample position and the oblique transmission of the sample by the neutron beam, the resolution in the position is low. Because of this low resolution, a constant gradient of the vortex distribution can not be concluded.

The remanence in the peak at 4.5 mm after field cooling is higher than the remanence in the other peak at 1.5 mm. Apparently the region near 4.5 mm contains more pinning centres per volume than the region at 1.5 mm and thus the distribution of the pin centres is not homogeneous.

The expulsion of vortices on a very short time scale (ms) can not adequately be described if only expulsion due to flux creep is taken into account. Also the expansion of the vortices right after the pulse has to be taken into account. During the first 100 ms after the puls, most vortices are expelled. In this time the vortex distribution is very chaotic. After that, the vortex distribution becomes more homogeneous as a function of time, which can be concluded from the observed decrease of the depolarization. Because the field in the sample is not directed in the direction of the main axes, a direction of largest chaos can not be determined.

A small angle between the external field and the crystallite platelets causes field components perpendicular to the crystallite platelets. if these perpendicular field components exceed a critical field H_{c1} the vortices will penetrate the crystallite. After the pulse most vortices will be expelled although some vortices will be remanent. These vortices rotate in the crystallite platelets due to dipole coupling of the supercurrents in the CuO-planes. Due to the combining of the x and y directed parts of vortices and the rotation of vortices in the crystallite planes, large x and y fields in the order of the z field will be formed. So it can be concluded that the texture of the sample can have considerable consequences for the vortex distribution.

References

[1] H. Kamerlingh Onnes, Comm. Phys. Lab. University of Leiden, Nos 119, 120, 122 (1911)

[2] J. Bardeen, L.N. Cooper and J.R. Schrieffer, Phys. Rev. 108, 1175 (1957)

[3] Sample made by V.A.M. Brabers, TU Eindhoven (1991)

[4] M.J.V. Menken, A.J.M. Winkelman, A.A. Menovsky, 'Crystal growth of Bi-based (85 K) high T_c superconductor compound with a mirrow furnace', Preprint

[5] C.P. Bean,'Magnetization of high field superconductors', Rev. of Modern Physics (1964)

[6] M.Th. Rekveldt, Z. Physik B259, (1973) 391; JMMM1, (1976) 342;

[7] Lecture notes 'Supergeleiding', c45, TU Delft, 1991

[8] R. Rosman, 'Magnetic particles studied with neutron depolarization and small angle neutron scattering, Chapter 5, Ph. D. Thesis, TU Delft, 1991

[9] W. Roest, M. Th. Rekveldt, Phys. Rev B, 48, 1993

[10] J.C. Phillips, Physics of high T_c superconductivity, p. 294

[11] B.Pumpin, M.Keller, W.Kundig, W.Odermatt, Phys. Rev. B, 42, 8019, 1990

[12] Z. Koziol, P. de Chatel, J.J.M. Franse'Evidence for the nonlinear flux diffusion from magnetization relaxation in $Bi_2Sr_2CaCu_2O_8$ single crystals, Preprint, 1992